

Electronic Thesis and Dissertation Repository

9-24-2018 10:00 AM

Development and validation of a stand-alone DCS system for monitoring absolute cerebral blood flow.

Mahro Khalid, *The University of Western Ontario*

Supervisor: St. Lawrence, Keith, *The University of Western Ontario*

A thesis submitted in partial fulfillment of the requirements for the Master of Science degree in Medical Biophysics

© Mahro Khalid 2018

Follow this and additional works at: <https://ir.lib.uwo.ca/etd>



Part of the [Medical Biophysics Commons](#)

Recommended Citation

Khalid, Mahro, "Development and validation of a stand-alone DCS system for monitoring absolute cerebral blood flow." (2018). *Electronic Thesis and Dissertation Repository*. 5752.
<https://ir.lib.uwo.ca/etd/5752>

This Dissertation/Thesis is brought to you for free and open access by Scholarship@Western. It has been accepted for inclusion in Electronic Thesis and Dissertation Repository by an authorized administrator of Scholarship@Western. For more information, please contact wlsadmin@uwo.ca.

Abstract

Premature infants are at high risk of neonatal brain injury due to poor cerebrovascular regulation, leading to periods of dangerously low cerebral blood flow (CBF) and possible injury. However, there are currently no established bedside methods of monitoring CBF to alert the intensive care staff to cerebrovascular dysfunction. Diffuse correlation spectroscopy (DCS) is an emerging noninvasive optical technique for monitoring relative CBF. I developed a stand-alone DCS method of monitoring absolute CBF by incorporating a quantitative dynamic contrast-enhanced (DCE) technique. This required modifying a DCS system to capture multi-distance data to measure the tissue optical properties and to perform DCE experiments. The feasibility of the technique was assessed by measuring CBF in piglets under three flow conditions. For validation, the tissue optical properties were compared to measurements from time-resolved near-infrared spectroscopy (NIRS). Across 7 animals, a strong linear correlation was observed between CBF values derived using the two sets of optical properties at baseline ($R^2=0.95$), hypercapnia ($R^2=0.83$) and hypocapnia ($R^2=0.88$). These results demonstrate that the developed DCS system provided the unique ability to provide real-time monitoring of absolute CBF.

Keywords

Diffuse correlation spectroscopy, NIRS, Optical diagnostics, medical imaging, spatially resolved NIRS, bolus tracking, neuromonitoring, neonates.

Acknowledgments

First and foremost, I would like to acknowledge my supervisor Dr. Keith St. Lawrence for providing me with opportunities which I otherwise would not have been afforded. I am forever indebted to him for providing me with the best guidance and understanding throughout my time at Western. His support and trust in me, not only helped in making my transition here easier, but it also made me feel at home here at Lawson.

Every part of this thesis is the result of the dedication and support of many individuals, who embodies the warm and receptive environment that I experienced here at Western. I cannot give enough thanks to Dr. Daniel Milej, who is both a mentor and a friend. His encouragement and positivity made challenges easier to deal with. Moreover, his dedication toward science and his sense of perceptiveness was an inspiration for me throughout. I undoubtedly will be indebted to him for playing a vital role in cultivating my research capabilities.

I have had the privilege of working with some of the best individuals here at Lawson. I feel grateful to have come across such welcoming and supportive colleagues and would like to extend my thanks to each and every individual I have had the pleasure to interact with. Particularly, I am grateful to Ajay Rajaram for his brotherly advices and scholarly insights, to Androu Abdalmalak, for his valued support and understanding and to Matthew Kewin, for being a perfect office colleague. I am also grateful to my current and past work colleagues (Lawrence Yip, Tracy Ssali, Seva Loussoufovitch, Marwan Shahid, Kyle Verdecchia and Uduuna Anazodo) for their friendship and for making London feel like home.

I would also like to thank my advisory committee members, Dr. Mamadou Diop and Dr. Kevin Shoemaker for providing me with support and guidance. My gratitude to the wonderful team of laboratory technicians including Laura Morrison, Jennifer Hadway, and Lise Desjardins cannot be overstated. Completion of work in this thesis would not be possible without their expertise and assistance in designing protocols and conducting animal experiments. Lastly, special thanks to my family here and back home for their love, understanding and support during this time.

Table of Contents

Abstract	i
Acknowledgments.....	ii
Table of Contents	iii
List of Tables	vi
List of Figures.....	vii
List of Appendices	ix
Abbreviations	x
Chapter 1	1
1 Introduction	1
1.1 Clinical Significance.....	1
1.2 Near Infrared Spectroscopy	3
1.3 Propagation of Light in Tissue.....	6
1.3.1 Radiative Transfer Equation	6
1.3.2 Diffusion Approximation.....	7
1.3.3 Modified Beer-Lambert Law	9
1.4 Near-Infrared Techniques	10
1.4.1 Continuous-Wave NIRS	11
1.4.2 Spatially Resolved NIRS	11
1.4.3 Time-Resolved NIRS.....	12
1.4.4 Frequency Domain NIRS.....	13
1.5 Dynamic Contrast-Enhanced NIRS to Measure CBF.....	14
1.6 Diffuse Correlation Spectroscopy.....	15
1.6.1 Intensity Autocorrelation and Correlation Diffusion Equation	16
1.6.2 DCS Models of Blood Flow $\langle r \rangle$	18

1.6.3	DCS System	18
1.7	Study Rationale	20
1.8	Research Objective:	21
Chapter 2	22
2	Methods	22
2.1	Animal Preparation	23
2.2	Experimental Procedure	24
2.3	Instrumentation	25
2.3.1	Diffuse Correlation Spectroscopy	25
2.3.2	Time-Resolved NIRS	27
2.4	Data Analysis	28
2.4.1	Measuring the Tissue Optical Properties by DCS and TR-NIRS	28
2.4.2	DCE Measurements of Absolute CBF	30
2.4.3	Dynamic CBF	31
2.5	Statistical Analysis	32
Chapter 3	33
3	Results	33
3.1	Physiological Parameters	33
3.2	Optical Properties	34
3.3	DCS and DCE Data Under Different Flow Conditions	36
3.4	CBF Measurements	37
3.5	Flow Changes During Change in Capnic Level:	40
Chapter 4	42
4	Discussion	42
Chapter 5	47
5	Conclusions and Future Work	47

References.....	50
Appendix A.....	54
Curriculum Vitae	55

List of Tables

Table 3-1: Average physiological parameters \pm standard deviation at baseline, hypercapnia and hypocapnia. * indicates significant difference relative to the baseline value.	33
Table 3-2: Optical properties \pm standard deviation calculated by TR-NIRS and MD-DCS of 7 animals at 802 nm and 785 nm. Values are presented at baseline for μ_s' and at baseline, hypercapnia and hypocapnia for μ_a	34
Table 3-3: CBF values (mean \pm standard deviation) calculated for 7 animals under baseline, hypercapnia and hypocapnia from optical properties derived from TR and MD.	38

List of Figures

Figure 1-1: Molar extinction coefficients for the three main endogenous chromophores: oxyhemoglobin (HbO₂), deoxyhemoglobin (HHb) and water..... 4

Figure 1-2: Measured IRF of the instrument and the measured dispersion of the photon arrival time after the light interrogates the tissue (TPSF)..... 13

Figure 1-3: A) Schematic of a multiple light scattering event inside a tissue, where light interact with the moving RBCs and is scattered, with the solid and dotted lines showing the path the light takes at time t and later after delay at $t+\tau$. B) Shows the intensity fluctuations detected by the detectors. C) Schematic shows the phase decay calculated based on the speed of the moving scatterers. 16

Figure 2-1: Software-based DCS system consisting of a 785 nm laser incident on the tissue surface and detectors placed 15, 20, and 25 mm from the source. Emitted light is scattered within the tissue and directed to APDs, which produced a train of TTL pulses that are fed into the counting board, which stores them in an internal buffer. The normalized autocorrelation curve is then computed. 26

Figure 2-2: TR-NIRS system consisting of a 802 nm picosecond laser placed 30 mm away from the detector on the piglet head. Detected light from the PMTs is transferred to the computer for computation of TPSFs..... 28

Figure 3-1: Regression plot (filled circles) comparing μ_s' values measured by TR-NIRS and MD-DCS. The solid line is the best-fit from linear regression (slope = 0.92, intercept = 0.056 cm⁻¹ and $R^2 = 0.87$). 35

Figure 3-2: Regression plot of μ_a measured by TR-NIRS and MD-DCS under the 3 capnic levels. The dashed line is the best-fit from linear regression (slope = 0.89, intercept = 0.048 cm⁻¹ and $R^2 = 0.70$). Data are presented as the mean \pm standard error. 36

Figure 3-3: (A) Typical normalized intensity autocorrelation functions and (B) the corresponding tissue ICG curves measured at baseline, hypercapnia and hypocapnia in one

animal. Each curve in (A) was obtained by averaging a set of curves over a 2 minute acquisition period..... 37

Figure 3-4: Regression values comparing CBF values derived from DCE data using optical properties from TR-NIRS and MD-DCS 39

Figure 3-5: Bland-Altman plot comparing the CBF measurements obtained using baseline optical properties from TR-NIRS and MD-DCS. Mean difference between the two methods is indicated by the solid line and the 95% confidence interval is demarcated by the dashed line..... 40

Figure 3-6: CBF time course during (A) a hypercapnia challenge and (B) a hypocapnic challenge of two animals. The vertical dotted line at 5 minutes indicates the end of baseline and start of the capnic challenge. 41

Figure L-1: Schematic of the software correlator operation showing the counter operation in the PCIe-6612 data acquisition board. (Adapted from Wang et al. 2016)..... 54

List of Appendices

Appendix A: Software correlator working 54

Abbreviations

ANOVA	Analysis of Variance
BF_1	Blood Flow Index
CA	Cerebral Autoregulation
CBF	Cerebral Blood Flow
CCAC	Canadian Council of Animal Care
CW	Continuous Wave
DA	Diffusion Approximation
DCE	Dynamic Contrast Enhanced
DCS	Diffuse Correlation Spectroscopy
DLS	Dynamic Light Scattering
HbO ₂	Oxyhemoglobin
HHb	Deoxy Hemoglobin
ICG	Indocyanine Green
IRF	Instrument Response Function
IVH	Intraventricular Hemorrhage
MBBL	Modified Beer Lambert Law
MD	Multi Distance
NIRS	Near Infrared Spectroscopy
PMT	Photomultiplier Tube
PVL	Periventricular Leukomalacia
RBCs	Red Blood Cells
RTE	Radiative Transport Equation
RR	Respiratory Rate
SPAD	Single Photon Avalanche Photodiode
SRS	Spatially Resolved Spectroscopy

TPSF	Temporal Spread Function
TR	Time Resolved

Chapter 1

1 Introduction

This chapter provides an overview of biomedical optics as applied to brain monitoring in the neonatal intensive care unit and the limitations of current methods. The principles of near-infrared spectroscopy (NIRS) and the methodology employed to measure cerebral blood flow (CBF) are outlined. Lastly, diffuse correlation spectroscopy (DCS), which is the focus of my thesis is presented.

1.1 Clinical Significance

According to the Canadian Institutes of Health Research, of the 390,000 babies who are born in Canada each year, nearly 8% are preterm births (less than 37 weeks of gestation). Preterm birth is associated with two-third of infant deaths in Canada. In addition, preterm infants are at a higher risk of brain injury, with 40-50% developing long-term cognitive and behavioral deficits and 5-10% developing major disabilities such as cerebral palsy [1].

The major forms of preterm brain injury are associated with damage to the cerebral vasculature. One of the most common is intraventricular hemorrhage (IVH), which arises in one-third of very preterm infants [2][3]. It refers to internal bleeding from the germinal matrix into the ventricles and adjacent brain tissue. In more than 90% of the cases, IVH occurs within the first 3 postnatal days, and it is a major risk factor for death and poor neurodevelopmental outcome. Despite advances in neonatal care, it remains a significant problem. The other major form of neonatal brain injury is periventricular leukomalacia

(PVL), which refers to ischemic injury in the white matter near the lateral ventricles [4]. The vulnerability of the preterm brain to these types of injury is believed to be a combination of cerebrovascular risk factors coupled with systematic factors, particularly the high incidence of hypotension. Cerebral autoregulation (CA) refers to the ability to maintain normal CBF despite fluctuations in arterial blood pressure. It is known that CA is impaired in preterm brain due to the immaturity of the cerebral vessels [5][6]. In addition, CBF is extremely low in the preterm brain [7], and infants who developed brain injury have lower CBF [8]. It is likely that the combination of these two factors makes the preterm brain susceptible to brain injury; i.e., hemorrhage during periods of hypertension and ischemia when blood pressure decreases.

The seminal study conducted by Soul et al. in 2007 used NIRS to show that cerebral pressure-passivity is common in the preterm brain [9]. This was performed by correlating changes in tissue oxygenation, used as an indirect marker of CBF, to fluctuations in arterial blood pressure. Their results demonstrated that 87 of the 90 preterm infants had periods of cerebral pressure-passivity; however, they did not find a correlation to brain injury. One possible explanation is that they only looked at relative CBF changes and were not able to define the true magnitude of changes in blood flow by monitoring tissue oxygenation. Therefore, to overcome the low predictive power of this technique and improve sensitivity, the ideal method should be able to quantify CBF in order to determine how low flow drops during pressure fluctuations. This would be analogous to assessing brain injury associated with ischemic stroke in adults since severity of injury depends on both the duration and value of ischemic flow[10].

1.2 Near Infrared Spectroscopy

Near infrared spectroscopy is a non-invasive optical technique used primarily to monitor tissue oxygenation. It utilizes light in the near-infrared region (700-1000 nm), known as the optical window[11]. Due to low absorption in this band, light can penetrate deeper into tissue compared to visible light, which has a penetration depth of only a few millimeters. The interaction of light with tissue is by scattering and absorption. The latter refers to the transfer of energy to an absorbing molecule by excitation of a vibrational state. That is, if the frequency of a photon equals the energy that is required by the molecules to transition to a higher energy state, then the photon is absorbed, otherwise it is scattered (i.e., re-emitted in another direction). Scattering and absorption are characterized by their respective exponential coefficients: μ_s for scattering and μ_a for absorption. These coefficients are the reciprocal of the distance a photon typically travels before it is either scattered or absorbed. In the NIR range, μ_s is approximately 100 times greater than μ_a , reflecting the low absorption and high scattering properties of tissue.

The first person to arithmetically define absorption in a non-scattering medium was Pierre Bouguer. He discovered that in a homogeneous medium the decrease in light intensity is related exponentially to μ_a and the distance between source and detector (ρ):

$$I = I_0 e^{-\mu_a \rho} \quad \mathbf{1-1}$$

where I_0 is the source light intensity and I is the measured light intensity. In 1852, August Beer observed that light absorption was proportional to the concentration (c_i) of a

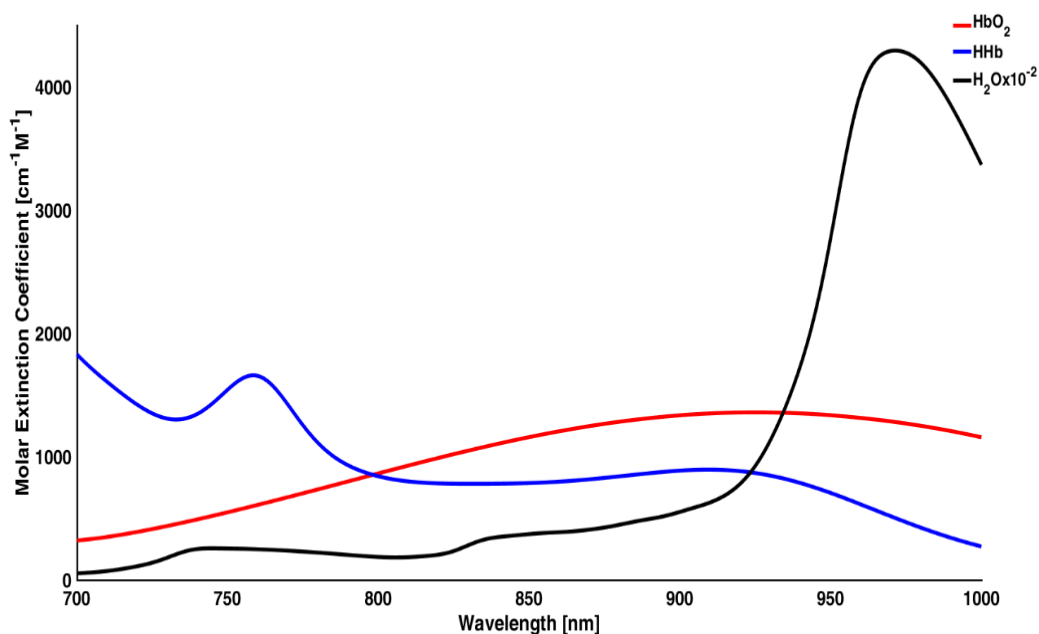


Figure 1-1: Molar extinction coefficients for the three main endogenous chromophores: oxyhemoglobin (HbO₂), deoxyhemoglobin (HHb) and water

chromophore (light-absorbing molecule) in the medium. In the presence of multiple chromophores, the absorption coefficient can be written as:

$$\mu_a(\lambda) = \ln(10) \sum_i \epsilon_i(\lambda) c_i \quad 1-2$$

where ϵ is the wavelength-dependent extinction coefficient of the i^{th} chromophore. Of all the chromophores in tissue, the main absorbing chromophores of NIR light are oxyhemoglobin, deoxyhemoglobin and water. Their wavelength-dependent absorption characteristics are illustrated in Figure 1-1.

Figure 1-1 highlights that the dominant tissue chromophore in the NIR region is hemoglobin, and the optical window is defined by the increase in absorption of hemoglobin at shorter wavelengths and by water at longer wavelengths. In principle, the concentration

of the main chromophores can be determined by applying Equation 1-2 to absorption data obtained at different wavelengths. However, the challenge to applying this approach to tissue is the much larger effects of light scattering.

In tissue, scattering is forward directed; however, the photon direction quickly becomes isotropic. This occurs at a distance given by $\sim 1/\mu_s'$, where μ_s' is defined as the reduced scattering coefficient and is defined as:

$$\mu_s'(\lambda) = (1 - g(\lambda)) \cdot \mu_s(\lambda) \quad \mathbf{1-3}$$

where g is the anisotropy factor, which is the average cosine of the scattering angle. It is a measure of the directionality of elastic scattering (i.e. scattering efficiency) and varies between -1 and 1.

Since tissue is a highly scattering medium, due to the presence of many scattering particles and changes in refractive indices within a small volume (1 mm^3), the number of scattering events is much higher than absorption interactions ($\mu_s' \gg \mu_a$). The main scattering constituents of a NIR photon, listed in order of scattering frequency, are lipoprotein membranes, mitochondria, red blood cells (RBCs), and other cellular components. These tissue scattering particles can be grouped into two categories: static and dynamic scatterers. The difference is the variation in phase of the interacting photon over time. Although scattering events occur more often with static tissue constituents, such as lipoprotein membranes and mitochondria, the phase change is time invariant, and the major contribution to the temporal phase fluctuations of a NIR photon is due to moving RBCs [12][13]. The variation in phase due to motion is an important phenomenon that can be exploited to measure flow.

1.3 Propagation of Light in Tissue

In biological tissues, scattering processes play a substantial role in the propagation of light. These scattered radiations contain information about tissue structural elements, their orientation, optical properties, and other parameters. To extract information and interpret experimental results, appropriate optical models for tissue based on radiation propagation are required.

1.3.1 Radiative Transfer Equation

Typically, the propagation of an electromagnetic wave in a medium can be solved using Maxwell's equations; however, in tissue the occurrence of many scattering events makes obtaining solutions to Maxwell's equations intractable. Due to this, simplification and different assumptions are needed to explain light propagation in tissue. Thus, when using Maxwell's equation, we approximate the solution by looking at light propagation as a stream of photons and by characterizing the individual photon pathlengths with radiative transport theory [14]. As radiance (the power of light emitted in a direction per unit solid angle [$\text{W}/\text{cm}^2/\text{sr}$]) travels within tissue, the radiative transport equation (RTE) mathematically models energy conservation by describing the interactions between particles and radiation:

$$\begin{aligned} \frac{1}{v} \frac{\partial}{\partial t} L(r, t, \Omega) + \hat{S} \cdot \nabla L(r, t, \Omega) + (\mu_a + \mu_s) L(r, t, \Omega) & \quad \mathbf{1-4} \\ = \mu_s \int_{4\pi} L(r, t, \Omega') P(\Omega, \Omega') d\Omega' + S(r, t, \Omega) \end{aligned}$$

where $L(r,t,\Omega)$ is the radiance in a medium at position r , traveling in direction Ω , at time t . The scattering phase function, $P(\Omega, \Omega')$, represents the probability of scattering into a direction Ω' from direction Ω . The speed of light in the medium is v , the source term is $S(r,t,\Omega)$, and $d\Omega'$ is the solid angle around Ω .

In an infinitesimal volume, the above equation accounts for the energy losses due to scattering and absorption, and energy gains because photon scattered into the volume and due to a light source. Even though this equation simplifies the Maxwell's equation, it is still complex and does not have analytical solutions. Therefore, further approximations are needed to solve the radiative transfer equation.

1.3.2 Diffusion Approximation

The diffusion approximation (DA) is one of the most widely used approximations to the radiative transfer equation. It is valid for conditions where the scattering length ($l_s=1/\mu_s$) is small compared to the distance of propagation. The standard approach to the diffusion approximation is through the P_N approximation, in which all angular dependent quantities (i.e. radiance, phase function, and light source) in a spherical Legendre series is truncated at the first order. The DA holds when the P_N assumes that the scattering coefficient is larger than the absorption coefficient, the observation point is far from the boundary of the medium, light is unpolarized, and the timescale is sufficiently long.

Thus, the photon fluence rate, which linearly combines the power of the photons incident on the sphere of cross-sectional area L [W/cm^2] can be written as:

$$\varphi(r, t) = \int L(r, t, \Omega) d\Omega \quad \mathbf{1-5}$$

and the photon flux, $J(r,t)$, defined as the vector sum of the radiance emerging from an infinitesimal volume [W/cm^2] is given by:

$$J(r, t) = \int \Omega \cdot L(r, t, \Omega) d\Omega \quad \mathbf{1-6}$$

The radiance from P_N approximation can also be derived independent of direction and is given by:

$$L(r, t, \Omega) = \frac{1}{4\pi} \varphi(r, t) + \frac{3}{4\pi} J(r, t) \Omega \quad \mathbf{1-7}$$

By combining the photon fluence with the radiative transfer equation and integrating over the solid angle, we get the continuity equation of the fluence rate:

$$\frac{1}{v} \frac{\partial}{\partial t} \varphi(r, t) + \nabla J(r, t) + \mu_a(r, t) \varphi(r, t) = S(r, t) \quad \mathbf{1-8}$$

The relationship between fluence rate and flux rate can be defined by Fick's law, which relates the diffusion of photons in a scattering medium by:

$$J(r, t) = -\frac{D(r, t)}{v} \nabla \varphi(r, t) \quad \mathbf{1-9}$$

$D(r,t)$ is the photon diffusion coefficient and is defined as:

$$D(r, t) = \frac{v}{3(\mu'_s + \mu_a)} \quad \mathbf{1-10}$$

Thus, in tissue the radiance of the RTE equation by photon fluence ($\varphi(r,t)$) can be described by the DA. It is derived by substituting Fick's Law into the fluence continuity equation to get:

$$\left(D(r, t)\nabla^2 - v\mu_a(r, t) - \frac{\partial}{\partial t}\right)\varphi(r, t) = -vS(r, t) \quad \mathbf{1-11}$$

The above equation can be used to characterize the paths travelled by photons that undergoes isotropic scattering, and unlike the RTE, analytical solutions are known for specific geometries.

1.3.3 Modified Beer-Lambert Law

Modified Beer-Lambert law (MBBL) is an empirical model that is widely used to analyze reflectance signal in NIRS applications. It uses continuous-wave diffuse optical intensity measurements to derive changes in tissue optical property. As compared to the Beer-Lambert law, which only accounts for tissue absorption, the MBBL accounts for light scattering by using the mean pathlength travelled by the photons through the highly scattering medium as the best estimate for the actual photon pathlength. The Modified Beer-Lambert law is derived from the first order Taylor expansion of the sample optical density (OD):

$$OD^0 \approx OD^0 + \left(\frac{\partial OD^0}{\partial \mu_a}\right)\Delta\mu_a + \left(\frac{\partial OD^0}{\partial \mu'_s}\right)\Delta\mu'_s \quad \mathbf{1-12}$$

where OD^0 is the baseline optical density, defined as the negative logarithm of the ratio of transmitted to incident light intensity:

$$OD = -\log\left[\frac{I_t}{I_0}\right] = \mu_0\rho \quad \mathbf{1-13}$$

where I_0 is the incident light, I_t is the transmitted light, ρ is the sample length and OD is proportional to the sample absorption coefficient (μ_a). The partial derivatives are evaluated at baseline condition, i.e. $\mu_a = \mu_a^0$ and $\mu'_s = \mu_s'^0$ and the differential changes in absorption and scattering are denoted by $\Delta\mu_a \equiv \mu_a(t) - \mu_a^0$ and $\Delta\mu_s \equiv \mu'_s(t) - \mu_s'^0$.

Based on these approximations, changes in optical density from baseline are given by:

$$OD = -\log\left(\frac{I_t}{I_0}\right) \approx \langle L \rangle \Delta\mu_a(t) + \left(\frac{\mu_a^0}{\mu_s^{\prime 0}}\right) \langle L \rangle \Delta\mu_s'(t) \approx \langle L \rangle \Delta\mu_a(t) \quad \mathbf{1-14}$$

The differential pathlength ($\langle L \rangle$) is the mean pathlength that diffusing photons travel within the medium from source to detector and is defined as:

$$\langle L \rangle \equiv \frac{\partial OD^0}{\partial \mu_a} \quad \mathbf{1-15}$$

Thus, using the above expansion, we can derive a Modified Beer-Lambert law for analysis of NIRS reflectance signal [15].

1.4 Near-Infrared Techniques

In clinical applications, NIRS data are acquired in either transmission or reflectance mode. In the former, the NIR light source is placed on one side of the medium, and the detector on the other side. Light is shone through the sample and collected after being scattered and absorbed. In reflectance mode, the NIR source and detector are placed on the same surface of the sample (such as the skin for in situ applications) and reflected photons collected are due to the high number of scattering events within the turbid medium. The latter technique is more common in neurological studies since the size of the human head makes it infeasible to collect information in transmission mode. Various NIR methods have been developed for this purpose and are described below.

1.4.1 Continuous-Wave NIRS

Continuous-wave (CW) NIRS is the simplest type of in vivo NIRS techniques, since it only measures the reduction in light intensity due to absorption and scattering in the medium. Generally, CW NIRS uses the modified Beer-Lambert Law to model light attenuation and changes in μ_a can be derived assuming scattering properties of the medium remain constant. Quantification of the concentration of the various chromophores is difficult with this simple approach since the differential pathlength is unknown and must be either assumed or measured by another method. [16]. Nevertheless, acquired attenuation data at multiple wavelengths (such as using multiple light emitting diodes) or across the NIR spectrum (using a broadband light source) can be used to monitor changes in the concentration of chromophores [17].

1.4.2 Spatially Resolved NIRS

Spatially resolved spectroscopy (SRS) is a CW method involving the acquisition of light intensity measurements at multiple source-detector distances [18][19]. For a semi-infinite homogeneous medium having a source defined as $r = 0$ and a detector placed at $r = r_{sd}$, the detected light intensity, known as the diffuse reflectance, is defined by the DA:

$$R_d(r_{sd}) = \frac{z_0}{2\pi} \frac{\exp\left[-\mu_{eff}(z_0^2 + r_{sd}^2)^{\frac{1}{2}}\right]}{z_0^2 + r_{sd}^2} \left[\mu_{eff} + \frac{1}{(z_0^2 + r_{sd}^2)^{\frac{1}{2}}} \right] \quad \mathbf{1-16}$$

where $z_0 = 1/\mu_s'$ describes the depth at which the direction of the emitted light becomes isotropic (i.e. entered the diffusion regime), and μ_{eff} is the effective attenuation coefficient:

$$\mu_{eff} \equiv \sqrt{3\mu_a(\mu_a + \mu'_s)} = \sqrt{3\mu_a\mu'_s} \quad \mathbf{1-17}$$

For a large source-detector distance (i.e. $r_{sd} \gg z_0$), the solution simplifies to:

$$\ln[r_{sd}^2 R_d(r_{sd})] = -\mu_{eff} r_{sd}^2 + \ln\left(\mu_{eff} + \frac{1}{r_{sd}^2}\right) + constant \quad \mathbf{1-18}$$

When $r_{sd} \gg \mu_{eff}$ the second term becomes a constant and a linear relationship is obtained between r_{sd} and $\ln[r_{sd}^2 R_d(r_{sd})]$, and the $-\mu_{eff}$ gives the slope of the equation:

$$\ln[r_{sd}^2 R_d(r_{sd})] = -\mu_{eff} r_{sd}^2 + intercept \quad \mathbf{1-19}$$

Thus, by plotting the intensities at different source-detector distance, we can get a direct estimate of μ_{eff} , which can be used to estimate μ_a assuming a known value of μ'_s .

1.4.3 Time-Resolved NIRS

Time-resolved (TR) NIRS uses lasers capable of emitting ultrashort pulses of light (of the order of picoseconds) and fast detectors capable of detecting the arrival of single reflected photons through the medium. A histogram of photon arrival times is generated, called the temporal point spread function (TPSF)[20][21]. It reflects the multiple different paths that photons take through the medium due to scattering. However, the measured TPSF is also influenced by the dispersion of light by the instrumentation. Therefore, the true distribution of the photon times of flight (called the DTOF) through the medium can only be obtained by removing the effects of the instrument response function (IRF) from the measured TPSF (Fig 1-2). Assuming the IRF is properly characterized, then the tissue optical properties

(μ_s' and μ_a) can be determined by modelling the DTOF by analytical solutions to the diffusion approximation.

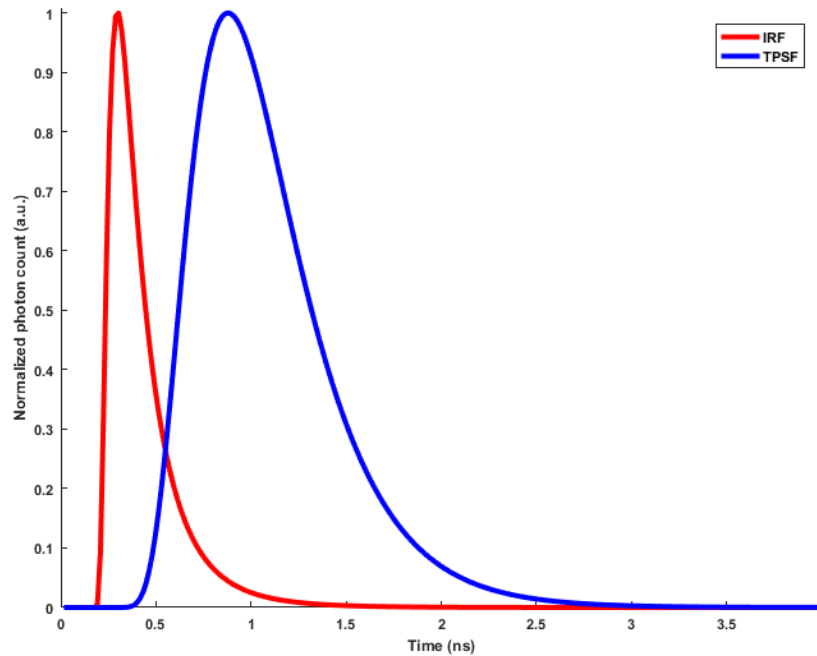


Figure 1-2: Measured IRF of the instrument and the measured dispersion of the photon arrival time after the light interrogates the tissue (TPSF)

1.4.4 Frequency Domain NIRS

Frequency domain NIRS can be considered the frequency analog of TR NIRS. With this approach, the light source is modulated at a known frequency, typically in the radio frequency range, and a fast detector is used to measure the change in light intensity (both DC and AC) as well as the phase shift between the emitted and detected light. The absorption and scattering coefficients can be determined by applying the DA to the measured phase shift and modulation amplitude in the frequency domain [22]. The

capability to collect phase information is the key difference between CW and frequency domain methods. However, phase measurements are inherently noisy, and frequency domain approaches require calibration against a tissue-mimicking phantom with known optical properties.

1.5 Dynamic Contrast-Enhanced NIRS to Measure CBF

Cerebral blood flow can be measured by NIRS using dynamic contrast-enhanced (DCE) techniques that rely on injecting of an optical contrast agent into the systemic circulation. The contrast agent acts as a blood flow tracer, whose transport through the microvasculature is modeled by constructing a kinetic model and applying it to the time dependent measurements of tracer concentration. The relationship relating the tissue concentration of contrast agent to its arterial blood concentration is given by:

$$C_t(t) = CBF \cdot \int_0^t C_a(t-u) \cdot R(u) du \quad \mathbf{1-20}$$

where $C_t(t)$ is the dye concentration in tissue as a function of time (t) measured by NIRS, $C_a(t)$ is the arterial blood concentration measured by a dye oximeter, and $R(t)$ is the impulse residual function, which represents the fraction of tracer in the tissue at time t , after an idealized bolus injection at time $t=0$ of unit concentration. The function $CBF \cdot R(t)$ can be extracted from the tissue and arterial ICG concentration curves by deconvolution. The initial height is equal to CBF since by definition $R(0) = 1$. Although this method is quantitative, it only provides a single CBF measurement and is therefore not suitable for continuous monitoring [23].

1.6 Diffuse Correlation Spectroscopy

Diffuse correlation spectroscopy (DCS) is an emerging non-invasive optical technique for monitoring tissue blood flow, which is similar to conventional NIRS, but it has the advantage of providing a continuous signal that is directly related to the movement of scatterers in tissue. DCS works by measuring the temporal correlation of coherent NIR light, which is dominated by the movement of red blood cells. It is an extension of dynamic light scattering (DLS), which follows single scattering events and is only applicable to optically thin samples. DCS, on the other hand, is a multiple scattering technique, which applies the methodology of DLS to thick samples. Here, individual scattering events combine to result in a net phase shift, which causes a decline in phase correlation. Because the primary moving light scatterers in tissue are RBCs, the measured phase changes are directly related to blood flow. However, DCS does not directly measure phase shifts, rather it measures temporal intensity fluctuations of coherent light, which are characterized by generating an autocorrelation function. In essence, faster moving RBCs lead to a more rapid loss of phase coherence, which is characterized by a rapid decrease in an autocorrelation function (Fig 1.2) [24][25].

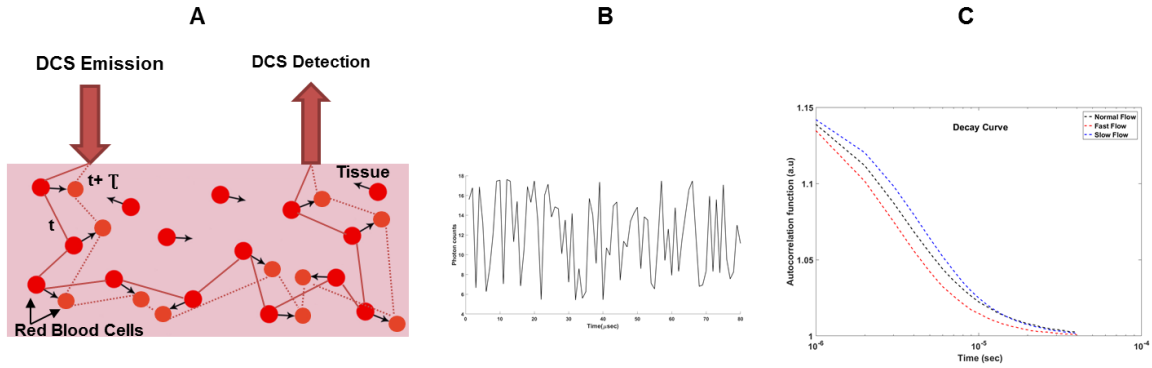


Figure 1-3: A) Schematic of a multiple light scattering event inside a tissue, where light interact with the moving RBCs and is scattered, with the solid and dotted lines showing the path the light takes at time t and later after delay at $t + \tau$. B) Shows the intensity fluctuations detected by the detectors. C) Schematic shows the phase decay calculated based on the speed of the moving scatterers.

1.6.1 Intensity Autocorrelation and Correlation Diffusion Equation

In a scattering medium, the normalized temporal autocorrelation function of an electric field ($E(t)$) is given by:

$$g_1 = \frac{\langle E(t) \cdot E^*(t + \tau) \rangle}{\langle |E(t)|^2 \rangle} \quad \mathbf{1-21}$$

where,

$$G_1 = \langle E(t) \cdot E^*(t + \tau) \rangle \quad \mathbf{1-22}$$

is the diffuse electric field autocorrelation function, τ is the autocorrelation delay time and $E(t + \tau)$ is the electric field after a delay τ . In DCS, temporal intensity fluctuations are measured rather than g_1 . The normalized intensity autocorrelation function, given by:

$$g_2 = \frac{\langle I(t) \cdot I^*(t + \tau) \rangle}{\langle |I(t)|^2 \rangle} \quad \mathbf{1-23}$$

where $I(t)$ is the light intensity detected at the tissue surface at time t . This normalized intensity autocorrelation function is related to $g_1(t)$ through the Siegert relationship:

$$g_2 = 1 + \beta |g_1(t)|^2 \quad \mathbf{1-24}$$

where β is the coherence factor of the detection system, which depends on the detection optics and is inversely proportional to the number of detected light modes.

Analogous to characterizing changes in light reflectance through a turbid medium, G_1 can be modelled using the diffusion approximation [26] [27]:

$$(D(r, t)\nabla^2 - v\mu_a(r, t) - k_D^2(\tau))G_1(r, \tau) = -vS(r, t) \quad \mathbf{1-25}$$

where

$$k_D^2(\tau) = 3\mu'_s\mu_a + \alpha\mu_s'^2 k_0^2 \langle r(\tau) \rangle \quad \mathbf{1-26}$$

accounts for the loss of correlation due to the motion of scatterers. $\langle r(\tau) \rangle$ is the mean-square displacement of the moving scatterers during a correlation time τ and is the proportion of moving scatters (largely RBCs in tissue), $k_0 = 2\pi n/\lambda$ is the wavenumber of light (λ is wavelength and n is the refractive index)[13]. In order to compute the $g_2(\rho, \tau)$ to estimate blood flow, an appropriate analytical model capable of mapping the tissue geometry and the motion of the erythrocytes in the tissue is required to solve for the correlation diffusion equation.

1.6.2 DCS Models of Blood Flow $\langle r \rangle$

Since the orientations of the microvessels in the brain are fairly random, dynamic scattering associated with red blood cells is commonly modeled as pseudo-Brownian motion. In this model, the mean square displacement, $\langle r(\tau) \rangle$, is equal to $6D_B$ where D_B is called the effective diffusion coefficient [28]. Using this definition, the solution to $G_1(\rho, \tau)$ for a semi-infinite homogeneous medium is given by:

$$G_1 = \frac{3\mu'_s}{4\pi} \left[\frac{\exp(-k_D r_1)}{r_1} - \frac{\exp(-k_D r_2)}{r_2} \right] \quad \mathbf{1-27}$$

where, $r_1 = [\rho^2 + z_0^2]^{\frac{1}{2}}$ and $r_2 = [\rho^2 + (z_0 + 2z_b)^2]^{\frac{1}{2}}$. z_0 is the effective depth of the source and is defined as $1/\mu'_s$, z_b is the extrapolated boundary and is defined as $2D(1+R_{eff}) \cdot (1-R_{eff}) - 1$. D is the diffusion coefficient and R_{eff} is the effective reflection coefficient given by 0.493 for the refraction indices of tissue and air [24][29]. It is common in DCS experiments to express the product αD_B as a blood flow index (BFI), which has units of cm^2/sec .

1.6.3 DCS System

The DCS system consists of a long coherence length laser that emits continuous near-infrared light at a particular wavelength. The output from the source is fed to a multimode fiber to deliver the light to the tissue. A long coherence length laser ensures that the emitted light is in phase for distances that are much greater than the typical photon pathlengths within tissue. A single-mode or a few-mode fiber is used to collect the reflected light, which

is directed to a suitable detector. Fast photon counting avalanche photodiodes, most commonly a single photon avalanche photodiode (SPAD) are used. The detector's output is fed into a correlator board that computes the normalized intensity autocorrelation function.

The most commonly used correlator board works on a multi-tau scheme, which was first introduced by Schatzel in 1985 [30]. Multi-tau schemes were developed to decrease computational load. The board takes the TTL signal to generate an autocorrelation function using a large range of delay times, ranging from 10ns up to hours. The correlator consists of registers (typically starting at 32 registers) with different bin width (T_0), which double after every few registers. When acquisition is initiated, a digital counter passes the photon counts as TTL pulses which are collected in time bins of the first register. This value is shifted to the right as each new value is updated from the left of the register. Each register is updated based on their T_0 value. Since T_0 doubles every few registers, the updating time for each register also varies with respect to T_0 . The temporal intensity autocorrelation function is calculated before each shift and the autocorrelation function is continuously averaged over the entire acquisition time t , whereas the delay time is the summation of all the bin widths on the left of the register. Using this technique, the computational load is greatly reduced as compared to the linear autocorrelator, but they do have limitations. For DCS applications, the lack of flexibility to compute over selected delay times makes hardware multi-tau correlators suboptimal since recorded correlation times are much smaller than the fixed ranged on the correlator board [31].

Recently, the development of software-based correlators has been proposed in order to provide a means of controlling the correlation times for DCS [32]. The approach feeds the

output of a SPAD into a high-speed counting board (PCIe-6612 National Instruments), which in turn is read by a high-level software program (LabVIEW) to compute autocorrelation functions with sub-second resolution. The advantage of this approach compared to a commercial hardware correlator, which measures correlation times over a wide and fixed range (1 μ s-1s), is the ability to measure only those correlation times relevant to blood flow (typically between 10 and 100 μ s). Targeting the optimal range greatly enhances the signal-to-noise ratio, thereby allowing measurements with millisecond resolution [32].

1.7 Study Rationale

DCS is an emerging noninvasive optical technique for monitoring relative CBF, but it does not provide a measure of absolute blood flow, making it difficult to assess if CBF drops to ischemic levels. To convert the DCS signal into units of CBF, it has been combined with DCE NIRS to estimate absolute flow. That is, a single value of CBF obtained using an optical contrast agent can be used to calibrate the BF_I data obtained by DCS [23]. This approach requires combining two optical systems: NIRS for measuring CBF, and DCS for monitoring BF_I , which adds to the complexity and cost of the system. Therefore, it would be advantageous to develop a stand-alone DCS system capable of monitoring absolute CBF. This device could be used to establish ischemic threshold in preterm infants as currently there is no means of determining the magnitude of CBF fluctuations in preterm infants with impaired CA.

1.8 Research Objective

The goal of my research work was to develop a portable system using DCS suitable for continuous monitoring and quantification of cerebral blood flow in preterm infants. To achieve this goal, the following objective were addressed:

1. Develop a stand-alone DCS system that incorporates a software correlator coupled to a multi-channel detection system in order to capture intensity and correlation data at multiple source-detector distance.
2. Validate the ability of the multi-distance (MD) DCS system to measure tissue optical properties in a neonatal animal model (piglets). Validation was performed by independently measuring the optical properties using TR-NIRS.
3. Demonstrate the ability of the system to track changes in CBF caused by altering arterial carbon dioxide pressure (i.e. both low (hypocapnia) and high (hypercapnia) conditions).

Chapter 2

2 Methods

The motivation for monitoring cerebral hemodynamics in the NICU was provided in Chapter 1. Ideally, the device should be portable and compact for bedside monitoring and provide a means of assessing CBF considering the link between blood flow instabilities and neonatal brain injury. This chapter outlines the development of a multi-distance DCS system designed for this purpose. The key modification to the system was the replacement of a hardware correlator with an in-house-developed software version. This enabled the acquisition of multi-distance intensity measurements to measure the tissue optical properties based on spatially resolved NIRS methodology. In addition, CBF was measured by acquiring DCE absorption changes using indocyanine green (ICG) as an intravascular contrast agent. By measuring absolute CBF, the DCS blood flow index could be converted into units of blood flow, enabling DCS to monitor CBF without requiring a separate NIRS system for the DCE experiments.

The experiments outlined in this chapter were conducted to test the sensitivity of the multi-distance DCS system to changes in CBF. Experiments were conducted in newborn piglets as the thickness of the extracerebral tissues (scalp and skull) is negligible, similar to preterm newborns. CBF was altered by manipulating arterial carbon dioxide tension (p_aCO_2): elevated p_aCO_2 (i.e., hypercapnia) to increase CBF and reduced p_aCO_2 (i.e., hypocapnia) to decrease CBF. In addition, the optical properties were measured

independently by TR-NIRS for comparison to measurements obtained by MD-DCS system.

2.1 Animal Preparation

Animal experiments were conducted in accordance with the guidelines of the Canadian Council of Animal Care (CCAC) and approved by the Animal Care Committee at Western University. Newborn piglets (<10 days old, 3.02 ± 1.37 kg, 4 females, 3 males) were initially anesthetized with 5% isoflurane, which was reduced to 3% for surgical procedures and maintained at 2-2.5% during the course of the experiment. Animals were tracheotomized and mechanically ventilated on a mixture of 2 L oxygen and 2 L medical air (21% O₂, balance N₂). Vital signs including heart rate (HR), end-tidal carbon dioxide tension, respiratory rate (RR), and blood pressure were continuously monitored (SurgiVet, Smith Medical, MN) via a femoral artery catheter. Arterial oxygen saturation was measured by a pulse oximeter attached to the piglet's right front hoof. Intermittent arterial blood samples were collected via the femoral catheter for blood gas and glucose analysis (Radiometer, ABL 80 FLEX CO-OX, Denmark). An ear and cephalic vein were catheterized for IV access, which included injecting ICG injections (Sigma-Aldrich, Saint Louis, MO) and infusing NaCl fluids (4 ml/kg/h). The piglet's scalp was shaved and the piglet was placed in a prone position within a plexiglass jig to help support a custom-made optical fiber probe holder, which held the DCS and TR-NIRS probes to the scalp throughout the experiment.

2.2 Experimental Procedure

The DCS optical fibers were positioned on the head at source-detector separations of 15, 20 and 25 mm. TR-NIRS optical fibers were placed parallel to the DCS holder, ensuring that they interrogated the same brain region, at a source-detector distance of 30 mm. Measurements from the two systems were acquired sequentially, with shutters placed in front of the TR-NIRS and DCS lasers, as well as the TR-NIRS photomultiplier tube (PMT). This prevented cross-talk between the two systems when collecting sequential data.

DCS and TR-NIRS data were acquired at each capnic level, starting with the baseline condition (normocapnia). At each level, TR-NIRS and MD-DCS data were collected to determine the tissue optical properties. In addition, DCE intensity data were collected with the DCS system in order to quantify CBF. The procedure involved a bolus injection of ICG (0.1 mg/kg in 1 ml of sterile water and dextrose used in equal ratio) into the ear vein, followed by acquiring a series of intensity measurements at a temporal resolution of 300 ms. At the same time, the time-varying arterial concentration curve was measured by a pulse dye densitometer (DDG 2001, Nihon Kohden, Tokyo, JP) attached to the right forelimb.

During the transition between capnic levels, DCS data were continuously recorded to track the dynamic changes in the BF_I . Measurements were taken for 20 minutes, encompassing a 5 minute period prior to CO_2 manipulation and 15 minutes following. The DCE protocol discussed above was performed at the end of each 20 minute period to measure CBF at the new p_aCO_2 value. Following each measurement, the animal's CO_2 level was returned to baseline before transitioning to a new state. To achieve hypercapnia, the piglet was

ventilated with 5.25% of CO₂ (0.5 L O₂ and 3.5 L CO₂) in order to accomplish a rapid change in capnic level, whereas hypocapnia was induced through hyperventilation to blow off CO₂. All experiments started at baseline and the order of hyper and hypocapnia was randomized.

2.3 Instrumentation

2.3.1 Diffuse Correlation Spectroscopy

The DCS system consisted of a long coherence length (>5 m) continuous-wave laser operating at 785 nm, with a maximum power output of 100 mW (DL-785-100-3S, CrystaLaser, Reno, NV). The laser was coupled to a multimode fiber (NA = 0.22, core = 400 μm, 4.7 mm outer diameter; Fiberoptics Technology, Connecticut, US) which directed the light to the head. The reflected light was collected by three 2.5 m long single-mode fibers (SMF-28-J9, NA = 0.14, core = 8.2 μm, single-mode cutoff wavelength = 1260 nm, Thorlabs, New Jersey, US) placed at 15, 20, and 25 mm source-detector distance and mounted to the head using a custom-designed 3D-printed probe holder. Each detection fiber was wrapped into a 15 cm coil to attenuate higher order modes by converting them into non-propagating modes [33][23]. Light from the detectors was received by a multi-channel single photon counting APD (SPCM-AQR-15-FC, PerkinElmer Canada Inc, Quebec, CA), which fed TTL pulses into an edge-detecting counter on a PCIe6612 counter/timer data acquisition board (National Instrument, Austin, Texas). Photon counts were recorded and processed using in-house developed software (LabVIEW, National Instrument and MATLAB) to generate intensity autocorrelation curves (g_2) (Fig 2.1).

The advantage of this approach compared to commercial hardware correlators, which measure correlation times over a wide and fixed range ($1 \mu\text{s} - 1 \text{s}$), is the ability to measure only those correlation times relevant to blood flow (typically between 10 and 100 μs). DCS measurements were conducted with a minimum baseline duration of 2 min at a temporal resolution of 300 ms; g_2 curves were computed using 40 delay time points (i.e. from 1 to 30 μs).

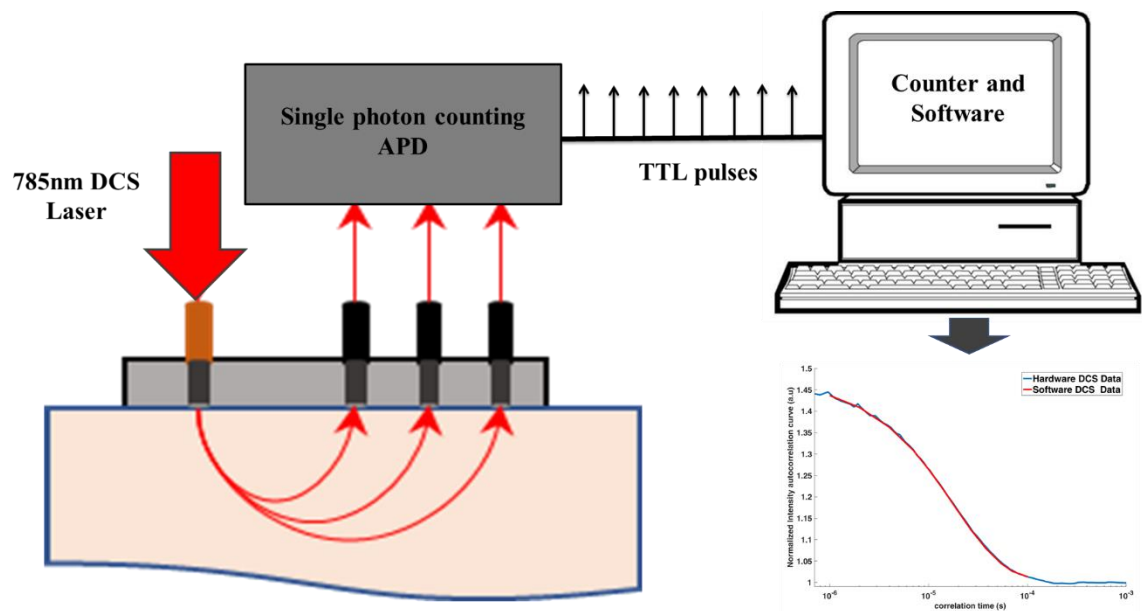


Figure 2-1: Software-based DCS system consisting of a 785 nm laser incident on the tissue surface and detectors placed 15, 20, and 25 mm from the source. Emitted light is scattered within the tissue and directed to APDs, which produced a train of TTL pulses that are fed into the counting board, which stores them in an internal buffer. The normalized autocorrelation curve is then computed.

The other advantage of developing a software correlator is that the photon count from each detector can be recorded. This, in addition to the baseline autocorrelation data, was used to measure the tissue optical properties as explained in the next section. Changes in the photon count were also recorded during the ICG bolus tracking measurements. In this case, the

temporal resolution was 300 ms and total acquisition time was 90 s. An intravenous bolus injection ICG was given at the 10 s mark.

2.3.2 Time-Resolved NIRS

The TR-NIRS system utilized a picosecond diode laser emitting at 802 nm (LDH-P-C-810, PicoQuant, Germany) (Figure 2-2). The output and pulse repetition rate of the laser were set to 1.4 mW and 80 MHz, respectively, through a computer-controlled laser driver (PDL 828, PicoQuant). The light was coupled into a multimode fiber (NA = 0.22, core = 400 μm , 4.7 mm outer diameter; Fiberoptics Technology, US) and directed towards the head. Reflected light was collected by a fiber bundle (core = 3600 μm , NA = 0.55, Fiberoptics Technology, United States) placed 30 mm from the emission fiber on the piglet's head. The collected photons were then sent to a hybrid photomultiplier tube (PMA Hybrid 50, PicoQuant, Germany), coupled to a HydraHarp 400 (PicoQuant, Germany) time-correlated single photon counting module to record the arrival times of the photons. TPSFs were computed using LabVIEW software. To measure the tissue optical properties, a TPSF was acquired over a 60 s period. The temporal dispersion caused by the system was corrected for by measuring the IRF. To avoid artifacts, such as instrument temporal drift, the TR-NIRS system was allowed 1 h to warm up prior to the experiment.

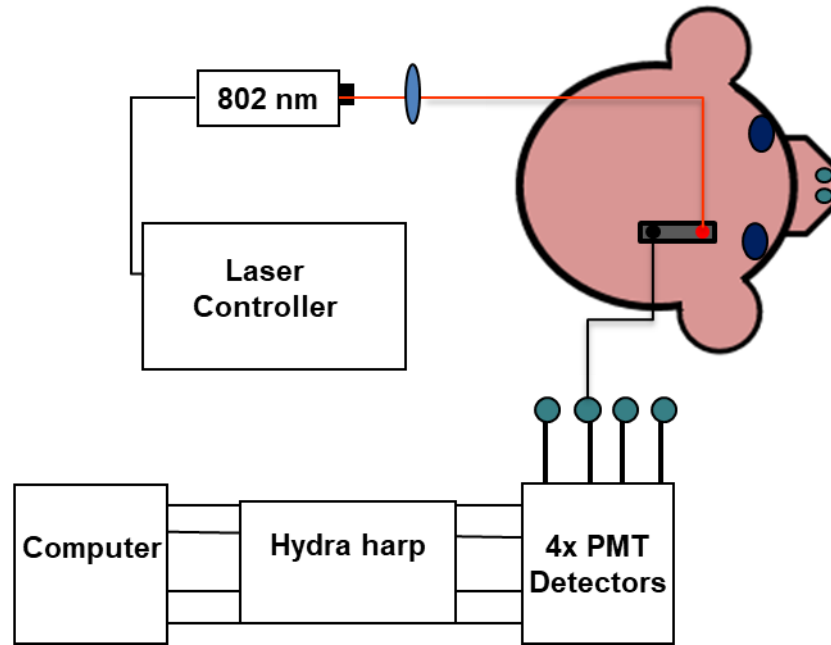


Figure 2-2: TR-NIRS system consisting of a 802 nm picosecond laser placed 30 mm away from the detector on the piglet head. Detected light from the PMTs is transferred to the computer for computation of TPSFs.

2.4 Data Analysis

2.4.1 Measuring the Tissue Optical Properties by DCS and TR-NIRS

To measure the tissue optical properties using MD-DCS, the effective attenuation coefficient (μ_{eff}) was determined from the light intensity measurements acquired at the different source-detector distances using the principals of spatially resolved NIRS, where μ_{eff} is given by:

$$\mu_{eff} = \sqrt{(3\mu'_s(\lambda) \cdot \mu_a(\lambda))}$$

2-1

μ_{eff} is the slope of intensity versus distance plot, as given by:

$$\ln[r_{sd}^2 \cdot I(r)] = -\mu_{eff} \cdot r_{sd} + I_0(0) \quad \mathbf{2-2}$$

where, $I(r)$ is the light intensity detected at a specific source-detector distance and I_0 is the light intensity at $r_{sd} = 0$.

The next step was to fit the acquired normalized intensity autocorrelation (g_2) curves, which were generated by the software correlator by:

$$g_2(\Delta n = \tau fs) = \frac{\langle n(i)n(i + \Delta n) \rangle}{\langle n(i) \rangle \langle n(i) \rangle} \quad \mathbf{2-3}$$

where $n(i)$ was the photon count at a time interval at index i on the internal buffer, f_s is the sampling frequency of the system operating at 1 MHz and $\langle \rangle$ represent the time averages over $n_{avg} = n_{total} - \Delta n$ points. The g_2 curves were fit using the solution to the correlation diffusion equation for a semi-infinite homogeneous medium, assuming Brownian motion of scatterers (as discussed in section 1.6):

$$G_1 = \frac{3\mu_s'}{4\pi} \left(\frac{e^{-k_D r_1}}{r_1} - \frac{e^{-k_D r_2}}{r_2} \right) \quad \mathbf{2-4}$$

where $k_D^2 = \mu_{eff}^2 + 6\mu_s' k_0^2 \alpha D_B \tau$. The term αD_B is the blood flow index. The two fitting parameters were μ_s' and αD_B with μ_{eff} set to the value from the spatially resolved analysis.

The final step was to determine μ_a from Equation 2-1 using the estimates of μ_s' and μ_{eff} .

To determine the optical properties by TR-NIRS, the measured TPSFs were fit using the solution to the diffusion equation for semi-infinite homogeneous medium using

extrapolated boundary conditions[34]. The IRF of the apparatus was also measured and convolved with the analytical solution. A non-linear optimization routine was used to fit the model convolved with the IRF to each measured TPSF [35]. All analyses were conducted using the MATLAB function `fminbound`.

2.4.2 DCE Measurements of Absolute CBF

The procedure underlying the bolus tracking technique for quantifying the CBF is based on measuring the change in signal intensity caused by the passage of ICG through the microvasculature. This approach models the ICG passage as a linear time-invariant system. That is, the time-varying concentration of ICG in tissue, $C(t)$, is linearly proportional to its concentration in arterial blood concentration, $C_a(t)$, and CBF is assumed constant during the measurement period, which is typically ~ 60 s. Based on these assumptions, $C(t)$ is related to $C_a(t)$ by the convolution operator:

$$C(t) = CBF \cdot \int_0^t C_a(t-u) \cdot R(u) du \quad \mathbf{2-5}$$

where $R(t)$ is the impulse residue function, which represents the fraction of ICG in tissue at time t following an ideal unit impulse injection at time $t = 0$. $C(t)$ was determined from intensity change due to the passage of ICG through the cerebral microvasculature as recorded by the multi-distance DCS system, and $C_a(t)$ was measured by the DDG (dye densitogram) as outlined in Section 2.2. The flow-scaled impulse residue function, $CBF \cdot R(t)$, was extracted from $C_a(t)$ and $C(t)$ by performing a deconvolution and its initial height is equivalent to CBF, since by definition $R(0) = 1$ [36].

$C(t)$ was determined using the solution to the diffusion approximation for a semi-infinite medium to extract the time-varying change in absorption, $\mu_a(t)$, from the intensity measurements at the largest source-detector distance:

$$C(t) = \frac{[(\mu_a(t) - \mu_a(0))]}{[\ln(10) \times \varepsilon_{ICG}]} \quad \mathbf{2-6}$$

where $\mu_a(0)$ represents the baseline absorption coefficient and ε_{ICG} is the extinction coefficient of ICG at 785 nm. The analysis required using the measured baseline optical properties, μ_a and μ_s' , as input parameters. For comparison, it was performed separately using the estimated of μ_a and μ_s' , from MD-DCS and from TR-NIRS. Changes in light absorption due to ICG were characterized using μ_a as a fitting parameter, while keeping μ_s' fixed to the baseline value.

2.4.3 Dynamic CBF

To determine the change in CBF from baseline to either hyper or hypocapnia, each g_2 curve in the time series between levels was fit to extract the BF_I (i.e., αDB) as a function of time. The value of CBF measured by the DCE method was used to convert the BF_I time series into units of CBF (ml/100g/min):

$$CBF(t) = \frac{BF_I(t)}{BF_{I0}} \times CBF_0 \quad \mathbf{2-7}$$

where $BF_I(t)$ is the flow index at time t , BF_{I0} is the baseline value, and CBF_0 is the value of blood flow determined by the DCE method.

2.5 Statistical Analysis

Statistical analyses were conducted using SPSS 17.0 (SPSS, Chicago, USA) and statistical significance was described as $p < 0.05$. Linear regression analyses were conducted to investigate the correlation between estimate of optical properties from TR-NIRS and MD DCS as well as the CBF values derived from the two sets of optical properties. An analysis of variance (ANOVA) was also used to determine the difference in optical properties between techniques and conditions. Finally, the degree of similarity between CBF measurements acquired by the two techniques was evaluated using a Bland-Altman plot [37]

Chapter 3

3 Results

3.1 Physiological Parameters

A total of 8 piglets were studied; however, one set was excluded due to poor quality of the baseline autocorrelation curves, resulting in no convergence in the fitting. The poor quality of this data set was attributed to poor contact of the probes on the piglet's scalp. Average values of the physiological parameters measured at each capnic condition from the seven successful experiments (4 females, 3 males, mean weight = 3.02 ± 1.37 kg, mean age = 6.7 ± 2.9 days) are summarized in Table 3-1.

Condition	p_aCO_2 (mmHg)	p_aO_2 (mmHg)	ctHb (g/dL)	HR (bpm)	MAP (mmHg)	pH
Baseline	39±2	230±76	7.1±1.2	157±16	47±2	7.39±0.02
Hypercapnia	63±5*	120±26*	7.4±1.13	189±31*	49±4	7.24±0.03*
Hypocapnia	28±2*	284±74*	7.3±1.5	168±15*	46±3	7.52±0.02*

Table 3-1: Average physiological parameters \pm standard deviation at baseline, hypercapnia and hypocapnia. * indicates significant difference relative to the baseline value.

(pH = arterial pH; p_aCO_2 = partial pressure of carbon dioxide in arterial blood; p_aO_2 = partial pressure of oxygen in arterial blood; ctHb = hemoglobin concentration; HR = heart rate; MAP = mean arterial pressure)

Of all the measured parameters, significant differences were observed in $paCO_2$, paO_2 , HR and pH under both conditions relative to baseline, whereas no significant difference in MAP or ctHb was noted under both conditions.

3.2 Optical Properties

Mean optical properties measured by MD-DCS and TR-NIRS are shown in Table 3-2. The scattering coefficient was calculated at baseline only, whereas the absorption coefficient was computed at baseline, hypercapnia and hypocapnia.

Technique	μ_s' (cm ⁻¹)	μ_a (cm ⁻¹)		
	Baseline	Baseline	Hypercapnia	Hypocapnia
TR-NIRS	7.51±1.59	0.11±0.02	0.13±0.02	0.12±0.01
MD-DCS	7.0±1.58	0.08±0.03	0.09±0.03	0.07±0.02

Table 3-2: Optical properties \pm standard deviation calculated by TR-NIRS and MD-DCS of 7 animals at 802 nm and 785 nm. Values are presented at baseline for μ_s' and at baseline, hypercapnia and hypocapnia for μ_a .

Figure 3.1 shows the regression plot of the baseline μ_s' values measured by TR-NIRS and MD-DCS. The graph revealed a strong linear correlation ($R^2=0.874$) between the μ_s' values from the two techniques with a slope of 0.93 and an intercept of 0.056 cm⁻¹.

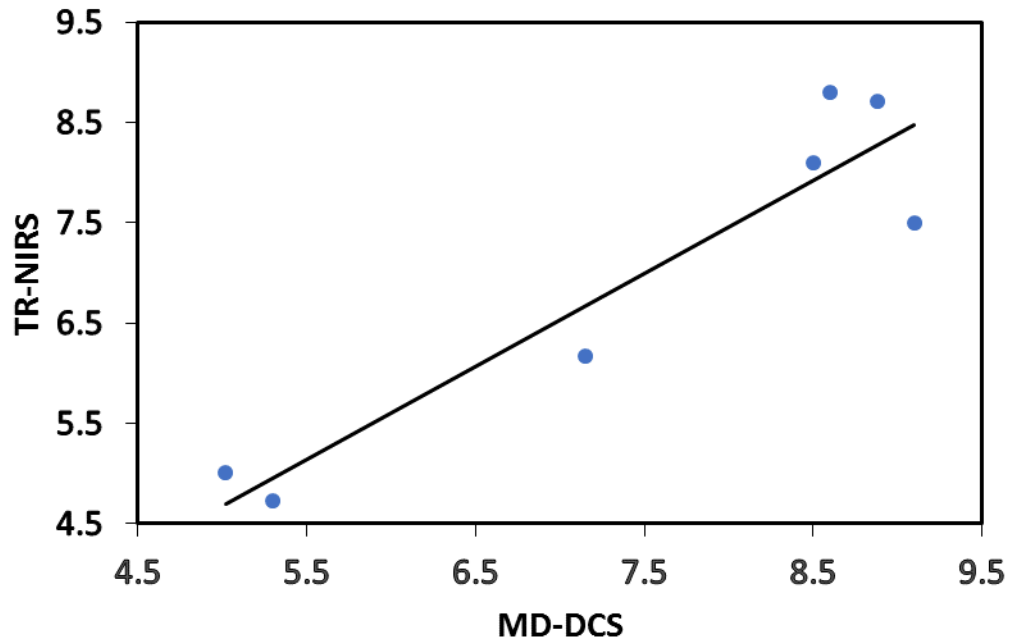


Figure 3-1: Regression plot (filled circles) comparing μ_s' values measured by TR-NIRS and MD-DCS. The solid line is the best-fit from linear regression (slope = 0.92, intercept = 0.056 cm^{-1} and $R^2 = 0.87$).

The correlation between mean values of the absorption coefficient measured by TR-NIRS and MD-DCS at the three capnic conditions is shown in Figure 3-2. The results showed a good correlation between the techniques ($R^2 = 0.70$, slope = 0.89 and a y-intercept = 0.048 cm^{-1}).

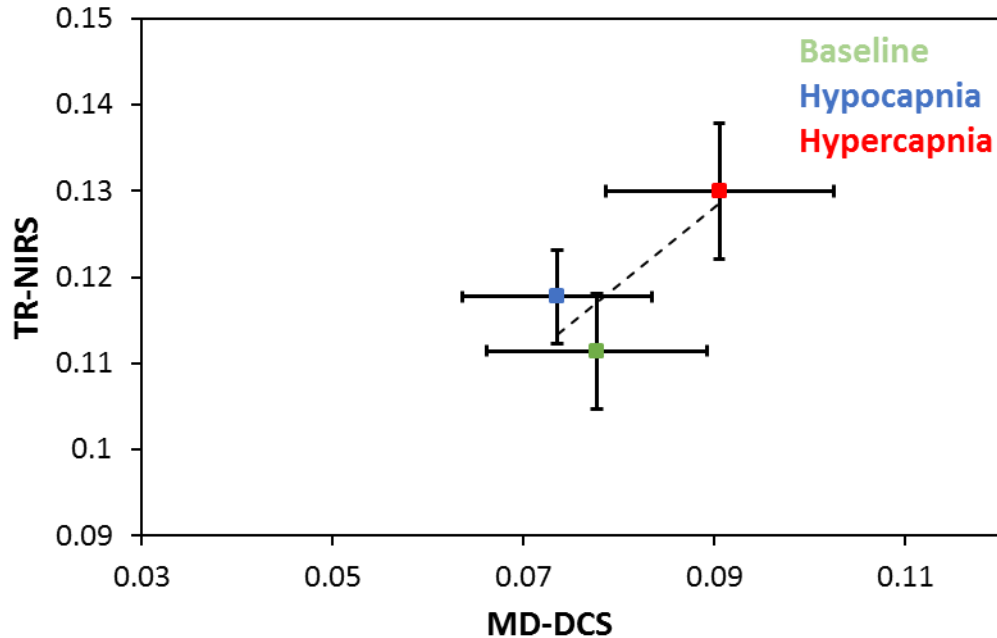


Figure 3-2: Regression plot of μ_a measured by TR-NIRS and MD-DCS under the 3 capnic levels. The dashed line is the best-fit from linear regression (slope = 0.89, intercept = 0.048 cm^{-1} and $R^2 = 0.70$). Data are presented as the mean \pm standard error.

The multi-variate ANOVA revealed two statistical effects on μ_a across conditions (baseline, hypercapnia and hypocapnia) and techniques (MD-DCS and TR-NIRS). That is, μ_a was significantly different across the three conditions ($F_{2,12} = 35.25$, $p < 0.05$) and significantly different between techniques ($F_{1,6} = 7.7$, $p < 0.05$).

3.3 DCS and DCE Data Under Different Flow Conditions

Measured normalized intensity autocorrelation functions and corresponding tissue ICG curves from one animal are shown in Figure 3.3. Data from each technique are shown under the three flow conditions: baseline, hypercapnia and hypocapnia. As expected, when CBF increased the autocorrelation curve decayed faster and visa-versa when blood flow

decreased. A similar trend was observed with the ICG tissue concentration curves. That is, the peak and initial rise of the first pass time both increased as CBF increased going from hypocapnia to hypercapnia.

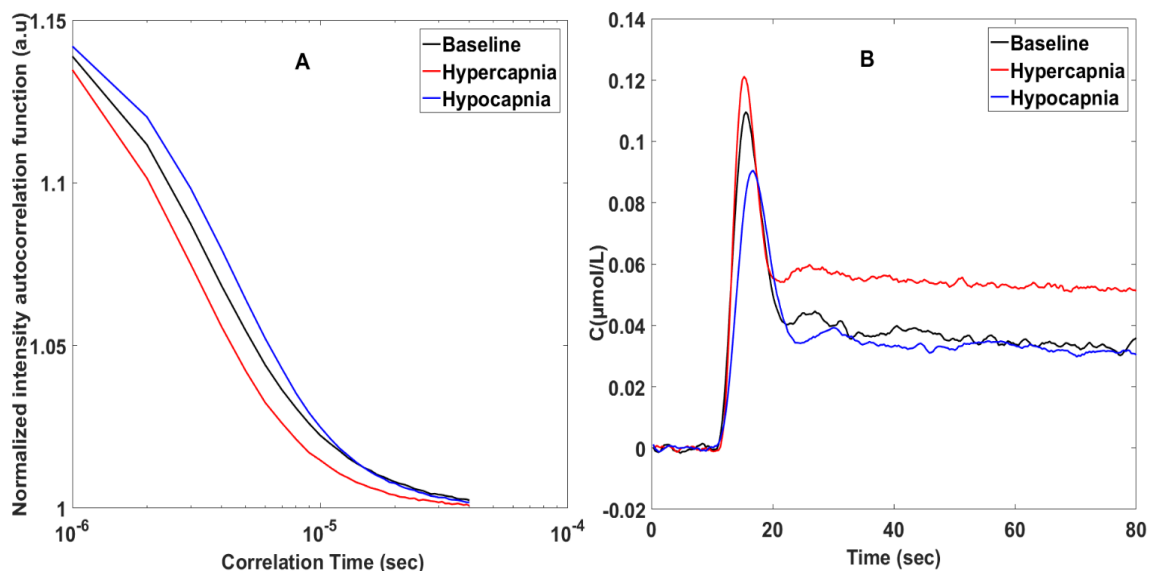


Figure 3-3: (A) Typical normalized intensity autocorrelation functions and (B) the corresponding tissue ICG curves measured at baseline, hypercapnia and hypocapnia in one animal. Each curve in (A) was obtained by averaging a set of curves over a 2 minute acquisition period.

3.4 CBF Measurements

Mean CBF values obtained from the DCE data using baseline optical properties measured by TR-NIRS and MD-DCS are shown in Table 3-3 for the three capnic conditions. Figure 3-4 shows the regression plot between the two sets of CBF values. A strong correlation was found with an $R^2 = 0.924$, slope of 0.91 and y-intercept of 4.27 ml/100g/min. The results of a multi-variate ANOVA revealed significant differences in CBF across

conditions ($F_{2,12} = 14.314$ and $p < 0.05$), but no significant difference between CBF values obtained with the two sets of optical properties.

Technique	Condition		
	Baseline	Hypercapnia	Hypocapnia
CBF_{TR-NIRS} (ml/100g/min)	28.03±14.43	37.31±10.63	19.69±6.25
CBF_{MD-DCS} (ml/100g/min)	26.34±14.70	35.54±12.32	17.44±6.58

Table 3-3: CBF values (mean ± standard deviation) calculated for 7 animals under baseline, hypercapnia and hypocapnia from optical properties derived from TR-NIRS and MD-DCS.

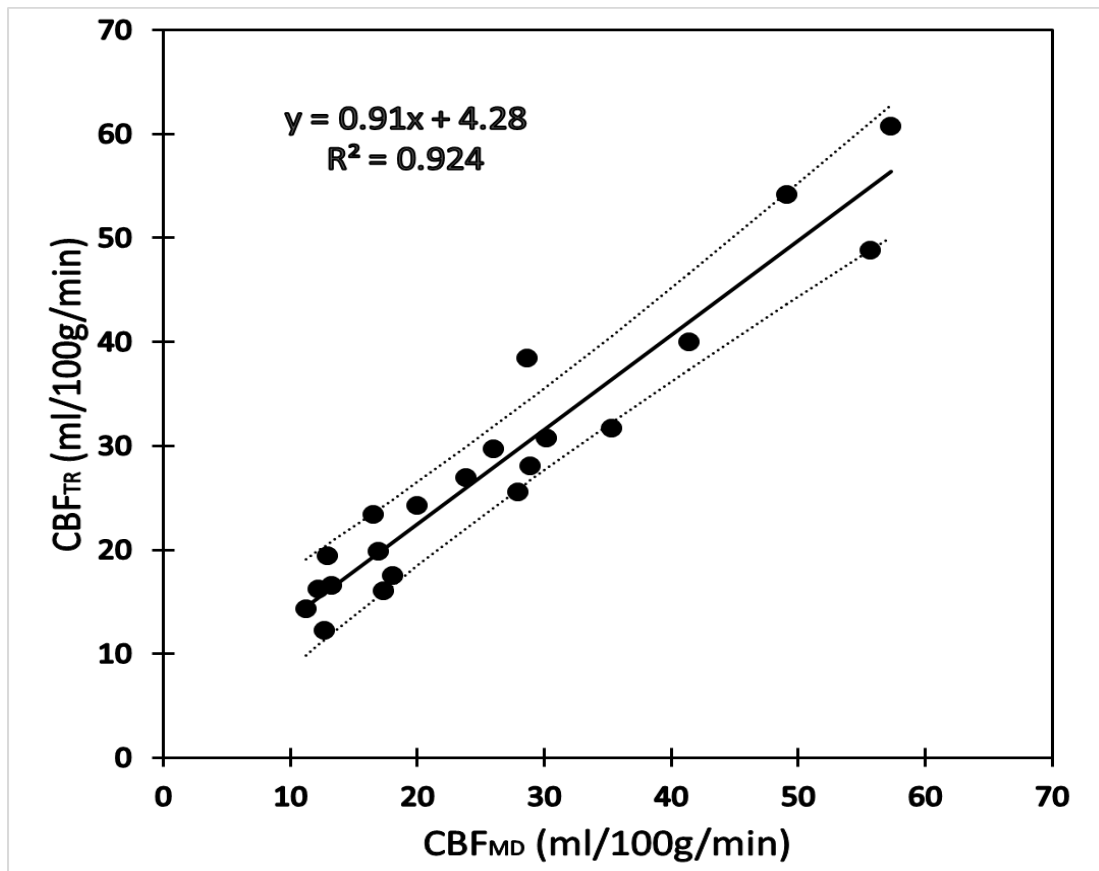


Figure 3-4: Regression values comparing CBF values derived from DCE data using optical properties from TR-NIRS and MD-DCS

Figure 3-5 shows the Bland-Altman plot comparing the two sets of CBF measurements.

The mean difference between both the techniques was 1.9 ml/100g/min, which was bound by 95% confidence intervals of -5.77 and 9.58 ml/100g/min.

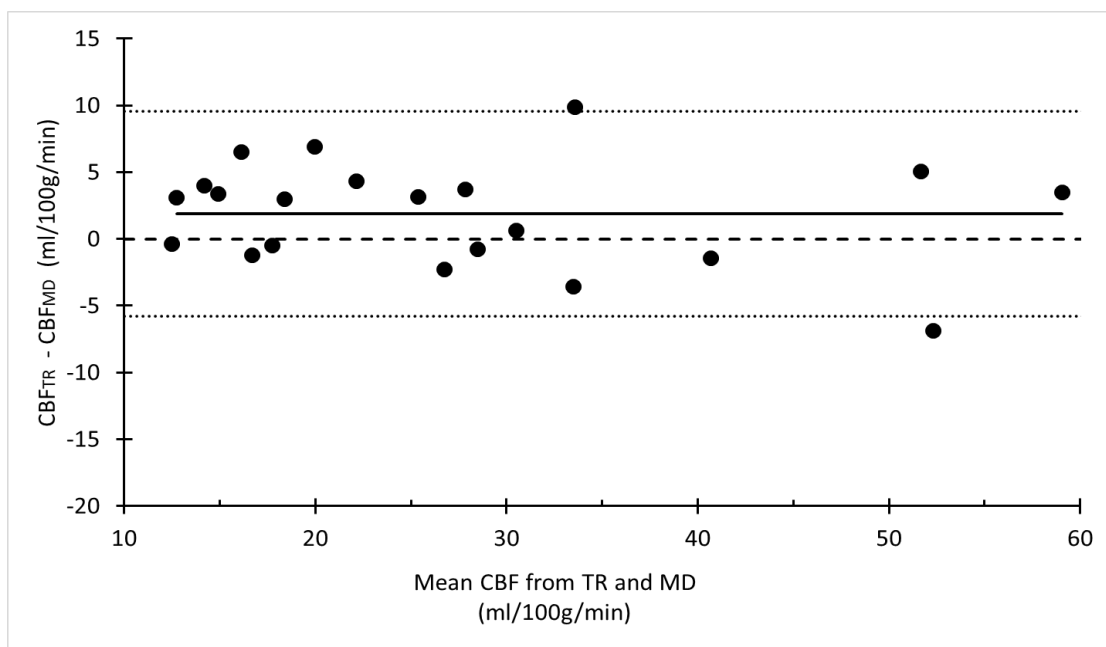


Figure 3-5: Bland-Altman plot comparing the CBF measurements obtained using baseline optical properties from TR-NIRS and MD-DCS. Mean difference between the two methods is indicated by the solid line and the 95% confidence interval is demarcated by the dashed line.

3.5 Flow Changes During Change in Capnic Level:

Illustrative plots of the temporal change in absolute CBF during the transitions from baseline to hypercapnia and to hypocapnia are shown in Figure 3-6. These CBF time plots are from separate animals and in each case the relative change in the blood flow index was converted to units of absolute CBF using a single baseline DCE measurement. The changes in blood flow from baseline to hypercapnia were more rapid than the corresponding change from baseline to hypocapnia because of the difference in how each capnic condition was induced. That is, hypercapnia was achieved by incorporating a small fraction of CO₂ into the breathing circuit, while hypocapnia was induced by hyperventilation.

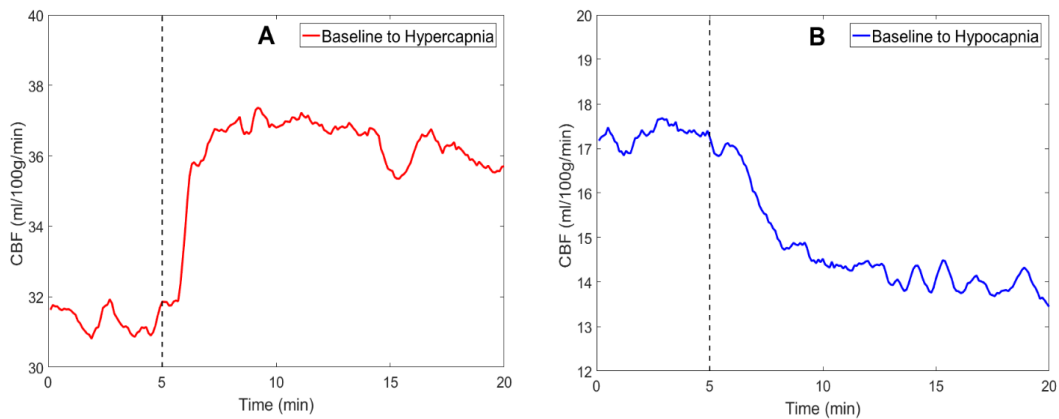


Figure 3-6: CBF time course during (A) a hypercapnia challenge and (B) a hypocapnic challenge of two animals. The vertical dotted line at 5 minutes indicates the end of baseline and start of the capnic challenge.

Chapter 4

4 Discussion

In this thesis, the development of a DCS system capable of measuring absolute CBF was presented. The key modification to an existing DCS system [24] was replacing a commercial hardware correlator with an in-house-developed software version that enabled the acquisition of light intensity and autocorrelation functions at multiple source-detector distances. The concept of using a software correlator for DCS was initially proposed to optimize the measured correlation times, thereby providing faster acquisition times [32],[38]. In this study, switching to a software correlator provided the ability to record light intensity, which was used to track the temporal changes in absorption caused by the passage of ICG through the cerebral vasculature. These changes were subsequently converted to a tissue ICG concentration curve using the baseline optical properties (μ_a and μ_s') derived by a combination of spatially resolved light intensity measurements and normalized intensity autocorrelation functions. The data presented in Figure 3.3 demonstrated that this approach could produce ICG concentration curves with high contrast to noise and was sensitive to blood flow changes. A previously validated deconvolution routine [23] was used to extract CBF from the recorded tissue and arterial ICG concentration curves. As a final step, the derived CBF value was used to convert relative blood flow data determined by DCS into units of absolute flow (e.g. Figure 3.6).

The concept of combining bolus-tracking and DCS techniques was first proposed by Diop et al. [23]. Using the same animal model as in the current study (newborn piglets), a strong

linear correlation between CBF measured by DCE-NIRS and the BF_I measured by DCS was reported ($R^2 = 0.93$) over a flow range from 17 to 90 ml/100g/min. This study highlighted the value of combining a quantitative NIRS method – in this case TR-NIRS – with DCS, as NIRS could be used to obtain the tissue optical properties and conduct a DCE experiment to determine CBF. The limitation was the need to combine two optical methods, which increases costs and the overall complexity of the system [23]. The MD-DCS approach developed in this thesis offers a less expensive and simpler alternative for monitoring CBF. Furthermore, it avoids any potential partial volume errors between optodes from separate systems and ensures the optical properties are measured at the same wavelength as the DCS data are acquired.

The first study to propose using MD-DCS to measure BF_I , μ_s' and μ_a was by Farzam et al. The idea was MD measurements would provide sufficient additional information to extract all three parameters. However, the signal-to-noise required to avoid crosstalk between the three fitting parameters limited the techniques to small source-detector separations (<2 cm) [39]. Recently, Tamborini et al. expanded this idea by acquired DCS data at both multiple wavelengths and source-detector separations to measure blood oxygenation and BF_I . Estimates of five fitting parameters (BF_I , two scattering terms, and concentrations of HbO and Hb) were obtained from a single cost function that included measurements of correlations times and light intensity at four source-detector distances and two wavelengths. Experiments involving tissue mimicking phantoms were used to demonstrate the importance of using both multi-distance and multi-wavelength measurements to accurately measure all fitting parameters, particularly μ_s' [40].

The current study followed a similar approach to Tamborini et al. by collecting intensity and correlation measurements at multiple source-detector distances. However, the focus was solely on measuring the baseline optical properties to derive tissue ICG concentration curves and not on estimating tissue oxygenation. Consequently, data were only recorded at a single wavelength, reducing the number of unknowns to BF_1 , μ_a and μ_s' . In addition, the two studies differed in how the MD intensity and correlation measurements were combined. In the current study, a three-step procedure was implemented: First, μ_{eff} was extracted from the MD intensity measurements, analogous to spatially resolved NIRS. Next, the intensity autocorrelation curves obtained at multiple source-detector distances were fit with the diffusion approximation (Equation 1.24), which involved only two parameters (μ_s' and BF_1) since μ_{eff} was determined in the first step. Finally, μ_a was estimated using Equation 2.1. The strong correlation between μ_s' estimates obtained by MD-DCS and TR-NIRS (figure 3.1) demonstrated that the former can measure μ_s' , despite the prediction by Tamborini et al. that data from multiple wavelengths are required. This is likely due to the difference in the number of fitting parameters used in the two approaches.

A correlation between μ_a estimates from MD-DCS and TR-NIRS (Figure 3.2) was also found; however, the μ_a values from MD-DCS were significantly lower than the corresponding TR-NIRS estimates, and the between-subject variation was approximately 70% greater for MD-DCS (Table 3.2). The most likely cause was errors in μ_{eff} considering the good agreement between μ_s' estimates from the two techniques. The primary assumptions of spatially resolved NIRS are that the tissue can be modelled as a semi-

infinite medium and the reflectance measurements are acquired on a flat surface. It is known that extracerebral tissues (scalp and skull) as well as cerebrospinal fluid in the subarachnoid space can affect the accuracy of spatially resolved measurements; however, the impact with respect to measurements on the piglet head should be minimal considering the depth to the brain from the skin surface is less than 3 mm [41]. The assumption of planer geometry can be violated if there is noticeable curvature to the head [42]. In the piglet experiments, the probes were positioned anteroposterior on one side of the head to achieve as closely as possible the required probe geometry. However, the dimensions of the piglet's cranium are relatively small and, therefore, some deviation was possible.

Despite the discrepancy in μ_a values between the two NIRS techniques, the CBF estimates obtained by analyzing the DCE data using the two sets of optical properties (Figure 3-4) were strongly correlated ($R^2 = 0.92$) and the mean bias from the Bland-Altman analysis was small (1.9 ml/100g/min). Furthermore, the variability between animals under each capnic condition was similar for the two sets of optical properties (Table 3-3). The CBF estimates did not show the variability observed with μ_a because the diffusion equation (Equation.1-16) used to obtain tissue ICG concentration curves is primarily dependent on μ_s' and μ_{eff} , and the latter is proportional to the square root of μ_a . These results indicate that the accuracy of the optical properties obtained from MD-DCS was sufficient for estimating CBF and a separate NIRS system specifically for measuring baseline μ_a and μ_s' is not necessary.

A potential complication with combining DCS with a bolus-tracking method is the effects of ICG on μ_a , which can affect BF_I measurements. To minimize this effect, each ICG

injection was followed by a 15-min delay to allow sufficient time for the dye to clear from the circulation. Previous experiments showed that the change in μ_a after the first pass of ICG is typically around 5%, which would translate into a 2% error in BF_I [23].

There are a number of potential limitations with this study. First, the optical properties measured by the two techniques were not at the same wavelength: TR-NIRS acquired data at 802 nm while and DCS measurements were at 785 nm. A previous study reported that this wavelength difference would lead to differences in optical properties of the order of 5% [23]. Second, TR-NIRS was only used to measure μ_a and μ_s' , and not to acquire a separate set of ICG concentration curves. The latter was not performed because the most direct means of measuring the absorption effects caused by the passage of ICG is by measuring the changes in light intensity. In contrast, TR-NIRS requires careful attention to ensure a linear relationship between dynamic absorption changes and the recorded distributions of times of flight [23].

Another potential limitation with the study was that hypercapnia was induced by adding 6% CO_2 to the inhaled gas mixture rather than altering the animal's breathing rate and volume, such as performed to induced hypocapnia. The former was conducted in order to elicit a rapid increase in $paCO_2$, which in turn would lead to a rapid CBF response. However, introducing the CO_2 tank into the breathing circuit required reducing the O_2 flow, which resulted in a significant drop in paO_2 relative to baseline (Table 3-1). Despite this decrease, paO_2 remained within normal limits and its effects on CBF would be small relatively to the large increase in $paCO_2$.

Chapter 5

5 Conclusions and Future Work

Based on the objective of developing a stand-alone DCE system capable of monitoring absolute CBF, I have:

1. Developed software to record intensity data and generate autocorrelation functions.
2. Modified a DCS system to record data at multiple distances using a multi-channel counter system.
3. Demonstrated the ability of the MD-DCS system to measure tissue optical properties, which were validated against TR-NIRS.
4. Presented experimental data results showing how the developed system can quantify CBF using a bolus tracking technique and can track changes in CBF.

Based on these results, a potential next step would be to conduct a clinical study to determine blood flow thresholds that are related to brain injury in preterm infants under intensive care. This would be analogous to studies of ischemic stroke in the mature brain that have shown that the extent of brain injury is related to both the drop in CBF and the duration of ischemia. Regarding neonatal brain injury, the goal would be to determine if there are flow thresholds in terms of the magnitude of the decrease in CBF and its duration that can be related to risk of brain injury (either IVH or PVL) developing. It is important to realize that normal CBF is considerably lower in the preterm brain relative to the mature brain and consequently specifically ischemic thresholds remain unknown in this

population. Hopefully, the MD-DCS approach developed in this work could help established critical ischemic thresholds.

An additional application of the MD-DCS system would be to use the improved temporal resolution provided by the software-correlator to capture flow pulsatility. Analogous to approaches based on transcranial Doppler, DCS measurements of flow pulsatility can be used to assess the critical closing pressure, which is the value of the arterial blood pressure at which CBF approaches zero [43]. The procedure does require blood pressure monitoring, which is performed in the neonatal intensive care unit. Investigating critical closing pressure in preterm infants has not seen a lot of attention, likely due in part to the lack of a suitable neuromonitoring technique.

The developed MD-DCS system used a single wavelength to measure the optical properties and CBF. Recent studies have shown that total hemoglobin concentration and oxygen saturation can be extracted by collecting DCS data at multiple wavelengths [40]. However, this requires developing a suitable laser drive to cycle between the two lasers that must provide suitable coherence to perform correlation analysis.

Finally, the present system targets neonates, who have negligible extracerebral signal contamination. Adapting this technology to adults would be challenging due to presence of extracerebral tissues that are of the order of 1 to 1.5 cm thick. The spatially resolved approach used to compute μ_{eff} is invalid for the adult head and therefore, translating this technology to adults would require an alternative approach. Recently, the concept of TR-DCS was proposed to combine DCS with the improved depth sensitivity of TR detection

[44]. However, the required technology is currently complex and requires more development.

In summary, the ability to continuously measure absolute flow could help improve the outcome of patients at risk of brain injury by early identification of abnormal CBF.

References

- [1] R. E. Behrman and A. S. Butler, Eds., *Preterm Birth: Causes, Consequences, and Prevention*. Washington (DC), (2007).
- [2] A. B. J. Stoll, N. I. Hansen, B. B. Poindexter, and N. N. Finer, “Neonatal Outcomes of Extremely Preterm Infants From the NICHD Neonatal Research Network,” **126**, (3), pp. 443–456, 2010.
- [3] S. Noori and I. Seri, “Hemodynamic antecedents of peri / intraventricular hemorrhage in very preterm neonates,” *Semin. Fetal Neonatal Med.*, **20**, (4), pp. 232–7, 2015.
- [4] Q. Shang, C.-Y. Ma, N. Lv, Z. Lv, Y. Yan, Z.-R. Wu, J.-J. Li, J.-L. Duan, and C.-L. Zhu, “Clinical study of cerebral palsy in 408 children with periventricular leukomalacia,” *Exp Ther Med*, **9**, (4), pp. 1336–1344, 2015.
- [5] G. Greisen, “Autoregulation of cerebral blood flow in new born babies.” *Early Human development*, **81**, (5) pp. 423–428, 2005.
- [6] E. S. Peebles, E. Mehic, P. D. Mourad, and S. E. Juul, “Fast Doppler as a novel bedside measure of cerebral perfusion in preterm infants,” *Pediatr. Res.*, **79**, (2), pp. 333–338, Feb. 2016.
- [7] L. Vutskits, “Cerebral blood flow in the neonate,” *Paediatr Anaesth*, **24**, (1), 2013.
- [8] J. H. Meek, L. Tyszczuk, C. E. Elwell, and J. S. Wyatt, “Low cerebral blood flow is a risk factor for severe intraventricular haemorrhage,” *Arch Dis Child Fetal Neonatal Ed*, **81**, (1) pp. 18–21, 1999.
- [9] J. S. Soul, P. E. Hammer, M. Tsuji, J. P. Saul, H. Bassan, C. Limperopoulos, D. N. Disalvo, M. Moore, P. Akins, S. Ringer, J. J. Volpe, J. Du Plessis, and F. Trachtenberg, “Fluctuating Pressure-Passivity Is Common in the Cerebral Circulation of Sick Premature Infants,” **61**, (4), 2007.
- [10] W.-D. Heiss, “The ischemic penumbra: how does tissue injury evolve?,” *Ann. N. Y. Acad. Sci.*, **1268**, pp. 26–34, Sep. 2012.
- [11] F. F. Jobsis, “Noninvasive, infrared monitoring of cerebral and myocardial oxygen sufficiency and circulatory parameters.,” *Science*, **198**, (4323), pp. 1264–1267, Dec. 1977.
- [12] T. Durduran, R. Choe, W. B. Baker, and A. G. Yodh, “Diffuse Optics for Tissue Monitoring and Tomography,” *Rep. Prog. Phys.*, **73**, (7), p. 76701, Jul. 2010.
- [13] R. Bonner and R. Nossal, “Model for laser Doppler measurements of blood flow in tissue,” *Appl. Opt.*, **20**, (12), pp. 2097–2107, 1981.
- [14] A. Ishimaru, “Diffusion of light in turbid material.,” *Appl. Opt.*, **28**, (12), pp. 2210–2215, Jun. 1989.
- [15] W. B. Baker, A. B. Parthasarathy, D. R. Busch, R. C. Mesquita, J. H. Greenberg, and A. G. Yodh, “Modified Beer-Lambert law for blood flow,” **5**, (11), pp. 4407–

4424, 2014.

- [16] A. Ghosh, C. Elwell, and M. Smith, “Review article: cerebral near-infrared spectroscopy in adults: a work in progress.,” *Anesth. Analg.*, **115**, (6), pp. 1373–1383, Dec. 2012.
- [17] A. Siegel, J. J. Marota, and D. Boas, “Design and evaluation of a continuous-wave diffuse optical tomography system.,” *Opt. Express*, **4**, (8), pp. 287–298, Apr. 1999.
- [18] S. Matcher, P. Kirkpatrick, K. Nahid, M. Cope, and D. T. Delpy, “Absolute quantification methods in tissue near-infrared spectroscopy, ” *Proc SPIE* **2389**. (1995).
- [19] H. Liu, D. A. Boas, Y. Zhang, A. G. Yodh, and B. Chance, “Determination of optical properties and blood oxygenation in tissue using continuous NIR light.,” *Phys. Med. Biol.*, **40**, (11), pp. 1983–1993, Nov. 1995.
- [20] D. T. Delpy, M. Cope, P. van der Zee, S. Arridge, S. Wray, and J. Wyatt, “Estimation of optical pathlength through tissue from direct time of flight measurement.,” *Phys. Med. Biol.*, **33**, (12), pp. 1433–1442, Dec. 1988.
- [21] B. Montcel, R. Chabrier, and P. Poulet, “Detection of cortical activation with time-resolved diffuse optical methods.,” *Appl. Opt.*, **44**, (10), pp. 1942–1947, Apr. 2005.
- [22] S. Fantini and M. A. Franceschin, “Frequency-domain techniques for tissue spectroscopy and imaging,” in *Handbook of optical biomedical diagnostics*, (2002), pp. 405–443.
- [23] M. Diop, K. Verdecchia, T.-Y. Lee, and K. St Lawrence, “Calibration of diffuse correlation spectroscopy with a time-resolved near-infrared technique to yield absolute cerebral blood flow measurements,” *Biomed. Opt. Express*, **2**, (7), p. 2068, 2011.
- [24] Guoqiang Yu; Durduran, Turgut; Zhou, Chao; Cheng, Ran; Yodh, “Near-Infrared Diffuse Correlation Spectroscopy for Assessment of Tissue Blood Flow,” in *Handbook of biomedical optics*, (2005), pp. 195–216.
- [25] D. A. Boas, L. E. Campbell, and A. G. Yodh, “Scattering and Imaging with Diffusing Temporal Field Correlations,” *Phys. Rev. Lett.*, **75**, (9), pp. 1855–1858, Aug. 1995.
- [26] D. A. Boas and A. G. Yodh, “Spatially varying dynamical properties of turbid media probed with diffusing temporal light correlation,” **14**, (1), pp. 192–215, 1997.
- [27] S. E. Skipetrov and R. Maynard, “Dynamic multiple scattering of light in multilayer turbid media,” *Phys. Lett. A*, **217**, (2), pp. 181–185, 1996.
- [28] K. Verdecchia, M. Diop, L. B. Morrison, T.-Y. Lee, and K. St. Lawrence, “Application of a Three-Layer Model to Multi-Distance Diffuse Correlation Spectroscopy: Validation Experiments in Pigs,” in *Biomedical Optics 2016*, (2016), p. JW3A.40.

- [29] K. Verdecchia, M. Diop, A. Lee, B. Morrison, Laura, T.-Y. Lee, and K. St. Lawrence, "Assessment of a multi-layered diffuse correlation spectroscopy method for monitoring cerebral blood flow in adults," *7*, (9), pp. 1951–1958, 2016.
- [30] K. Schätzel, "Correlation techniques in dynamic light scattering," *Appl. Phys. B*, **42**, (4), pp. 193–213, 1987.
- [31] D. Magatti and F. Ferri, "Fast multi-tau real-time software correlator for dynamic light scattering," **40**, (24), pp. 4011–4021, 2001.
- [32] D. Wang, A. B. Parthasarathy, W. B. Baker, K. Gannon, V. Kavuri, T. Ko, S. Schenkel, Z. Li, Z. Li, M. T. Mullen, J. A. Detre, and A. G. Yodh, "Fast blood flow monitoring in deep tissues with real-time software correlators," *Biomed. Opt. Express*, **7**, (3), p. 776, 2016.
- [33] G. Dietsche, M. Ninck, C. Ortoft, J. Li, F. Jaillon, and T. Gisler, "Fiber-based multispeckle detection for time-resolved diffusing-wave spectroscopy: characterization and application to blood flow detection in deep tissue.," *Appl. Opt.*, **46**, (35), pp. 8506–8514, Dec. 2007.
- [34] A. Kienle and M. S. Patterson, "time-resolved diffusion equations for reflectance from a semi-infinite turbid medium," **14**, (1), pp. 246–254, 1997.
- [35] A. Liebert, H. Wabnitz, D. Grosenick, and R. Macdonald, "Fiber dispersion in time domain measurements compromising the accuracy of determination of optical properties of strongly scattering media.," *J. Biomed. Opt.*, **8**, (3), pp. 512–516, Jul. 2003.
- [36] D. W. Brown, P. A. Picot, J. G. Naeini, R. Springett, D. T. Delpy, and T.-Y. Lee, "Quantitative near infrared spectroscopy measurement of cerebral hemodynamics in newborn piglets.," *Pediatr. Res.*, **51**, (5), pp. 564–570, May 2002.
- [37] J. M. Bland and D. G. Altman, "Statistical methods for assessing agreement between two methods of clinical measurement.," *Lancet (London, England)*, **1**, (8476), pp. 307–310, Feb. 1986.
- [38] D. Magatti, F. Ferri, and I. Introduction, "25 ns software correlator for photon and fluorescence correlation spectroscopy," **74**, (2), pp. 1135–1144, 2003.
- [39] P. Farzam and T. Durduran, "Multidistance diffuse correlation spectroscopy for simultaneous estimation of absolute scattering and absorption coefficient and the blood flow index," *J. Biomed. Opt.*, **20**, (5), p. 55001, 2015.
- [40] D. Tamborini, P. Farzam, B. Zimmermann, K.-C. Wu, D. A. Boas, and M. A. Franceschini, "Development and characterization of a multidistance and multiwavelength diffuse correlation spectroscopy system," *Neurophotonics*, **5**, (1), p. 1, 2017.
- [41] M. Diop, J. T. Elliott, K. M. Tichauer, T.-Y. Lee, and K. St. Lawrence, "A broadband continuous-wave multichannel near-infrared system for measuring regional cerebral blood flow and oxygen consumption in newborn piglets.," *Rev. Sci. Instrum.*, **80**, (5), p. 54302, May 2009.
- [42] M. Dehaes, L. Gagnon, F. Lesage, M. Pelegriani-Issac, A. Vignaud, R. Valabregue,

- R. Grebe, F. Wallois, and H. Benali, “Quantitative investigation of the effect of the extra-cerebral vasculature in diffuse optical imaging: a simulation study.,” *Biomed. Opt. Express*, **2**, (3), pp. 680–695, Feb. 2011.
- [43] R. B. Panerai, “The critical closing pressure of the cerebral circulation.,” *Med. Eng. Phys.*, **25**, (8), pp. 621–632, Oct. 2003.
- [44] J. Sutin, B. Zimmerman, D. Tyulmankov, D. Tamborini, K.-C. Wu, J. Selb, A. Gulinatti, I. Rech, A. Tosi, D. A. Boas, and M. A. Franceschini, “Time-domain diffuse correlation spectroscopy,” **3**, (9), 2016.

Appendix A

The software correlator used in this thesis was adapted from the work presented by Wang et al [32]. It was implemented on a standard personal computer using a PCIe 6612 counter/timer data acquisition board (National instruments, Texas, US) and a customized software program (LabVIEW, National Instruments, Texas, US). As shown in the schematic below, the digital pulses from each of the three channels generated by the photon counting APDs were transferred to three of the 8 edge-detecting photon counters on the PCIe board. The counters were synchronized by an internal timebase of 80 MHz, which updated its internal count by one when a TTL pulse was detected. These counts were then transferred to the internal buffer at a pre-defined sampling frequency of 1 MHz, which defines the bin width of the internal buffer ($f_s=1/\Delta t$). The counts were stored in the buffer ($N(i)$) at a pre-set temporal resolution of 300 ms given by t_{int} . The number of points on the buffer ($n_{int} = f_s \times t_{int}$) were transferred to the computer for storage, which were subsequently used to compute the autocorrelation function at each source-detector distance using Equation 2-3. The LabVIEW software computed the normalized intensity autocorrelation in real time using a buffered producer-consumer loop over 40 delay times that ranged from 1 to 30 μ s.

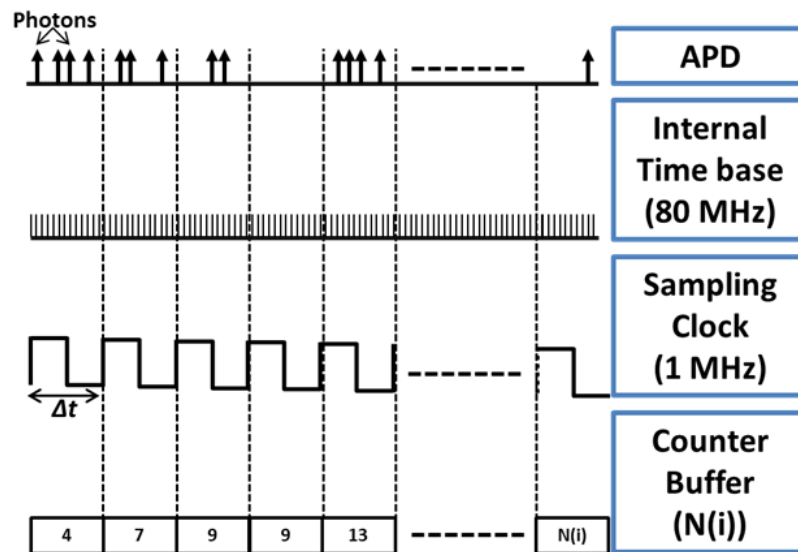


Figure L-1: Schematic of the software correlator operation showing the counter operation in the PCIe-6612 data acquisition board. (Adapted from Wang et al. 2016)

Curriculum Vitae

EDUCATION

Western University , Schulich School of Medicine and Dentistry MSc. Candidate in Medical Biophysics	2016-2018
NED University of Engineering and Technology , B.Eng. in Biomedical Engineering	2010-2015

RESEARCH & WORK EXPERIENCE

NED University of Engineering and Technology <i>Undergraduate senior thesis under Dr. Saad Abdullah</i>	2014-2015
Jinnah Postgraduate Medical Centre , Road Traffic Injury Research Centre <i>Research Intern</i>	2013
Aga Khan University Hospital , Biomedical Department <i>Biomedical Engineering Intern</i>	2012

AWARDS AND SCHOLARSHIPS

- Western Graduate Research Scholarship, Western University – Institutional competition (2016-2018, \$21,600)
- Biomedical Engineering Gold Medalist, NED University of Engineering and Technology– Departmental award (2015)
- NED University Graduate Scholarship Award, NED University – Interdepartmental competition (2011-2014)
- Dean’s Honour List, NED University (2011-2014)

PUBLICATIONS

Shahid H, Abdullah S, Mohani SZ, Khalid M, Khan MA "A Method of Operating a Microscope over Internet for Remotely Viewing and Analyzing the Slides - Remote telemicroscopy." J Med Diagn Meth S2:004 (December 2015)

PUBLISHED ABSTRACTS

1. Mahro Khalid, Daniel F Milej, Ajay Rajaram, Androu Abdalmalak, Mamadou Diop, Keith St Lawrence “*Self-calibrated DCS for monitoring of absolute cerebral blood flow*” Optical Society of America - Microscopy Histopathology and Analytics. JTU3A. 63. (2018)

2. Daniel Milej, Androu Abdalmalak, Mahro Khalid, Marwan Shahid, Ajay Rajaram, Matthew Kewin, Mamadou Diop, Keith St Lawrence “*Assessing Extracerebral Signal Contamination in NIRS and DCS.*” Society of Functional Near Infrared Spectroscopy (2018)

CONFERENCE PRESENTATIONS

1. **SPIE BiOS Photonics West** (International/TBD Presentation)
Marwan Shahid, Daniel Milej, Androu Abdalmalak, Ajay Rajaram, Mahro Khalid, Mamadou Diop, Keith St. Lawrence. “*Development of a hybrid optical system to study dynamic blood flow/oxygenation regulation in the human brain.*” (San Francisco, CA, 2019)
2. **Functional-NIRS Tokyo** (International/Poster Presentation)
Daniel Milej, Androu Abdalmalak, Mahro Khalid, Marwan Shahid, Ajay Rajaram, Matthew Kewin, Mamadou Diop, Keith St. Lawrence. “*Assessing extracerebral signal contamination in NIRS and DCS*” (Toyko, Japan, 2018)
3. **London Health Research Day** (Local/Poster Presentation)
Mahro Khalid, Daniel F Milej, Ajay Rajaram, Androu Abdalmalak, Mamadou Diop, Keith St Lawrence. “*Monitoring absolute cerebral blood flow using a self-calibrated software-based DCS system.*” (London, ON, 2018)
4. **Imaging Network Ontario** (Provincial/Poster presentation)
Mahro Khalid, Daniel F Milej, Ajay Rajaram, Androu Abdalmalak, Mamadou Diop, Keith St Lawrence. “*Development of a self-calibrated DCS for tracking absolute cerebral blood flow.*” (Toronto, ON, 2018)
5. **Optical Society of America** (International/Poster presentation)
Mahro Khalid, Daniel F Milej, Ajay Rajaram, Androu Abdalmalak, Mamadou Diop, Keith St Lawrence. “*Self-calibrated DCS for monitoring absolute cerebral blood flow.*” (Hollywood, FL, 2018)